

2

3 Revisiting the source rupture process of the mainshock of the 2016
4 Kumamoto earthquake and implications for the generation of near-
5 fault ground motions and forward directivity pulses

6

7 Kimiyuki Asano^{1,*} and Tomotaka Iwata¹

8

9 ¹Disaster Prevention Research Institute, Kyoto University, Gokasho, Uji, Kyoto 611-0011,

10 Japan

11

12 *Corresponding author: Kimiyuki Asano (k-asano@sms.dpri.kyoto-u.ac.jp)

13

14 Declaration of Competing Interests: The authors acknowledge there are no conflicts of

15 interest recorded.

16 **ABSTRACT**

17 Strong near-fault ground motions associated with the M_{JMA} 7.3 mainshock of the 2016
18 Kumamoto earthquake sequence, central Kyushu, Japan, have received attention by
19 seismological and engineering communities. In this study, the kinematic source rupture process
20 was reanalyzed based on an improved approach for the representation of source faults. The
21 slips at densely distributed point sources were defined via the bilinear interpolation of those at
22 surrounding control points. The result shows that the rupture started on the Hinagu fault with
23 a small initial rupture and propagated beyond the junction to the Futagawa fault. The rupture
24 on the Futagawa fault mainly propagated up- and northeastward. A large slip area with a peak
25 slip of 4.9 m and peak slip-velocity of 3.1 m/s was detected at depths ranging from 3 to 15 km
26 in the central part of the Futagawa fault. This asperity spatially coincides with a body with
27 moderate seismic velocity ($V_P \sim 6$ km/s) and low seismic attenuation. The slips on the Futagawa
28 fault have significant normal-slip components, whereas the slip vectors of the Hinagu fault
29 represent almost pure right-lateral strike-slip. The shallower part of the fault segments in the
30 western Aso caldera is characterized by relatively large normal slips. The estimated slip
31 velocity functions at shallower depths (<3 km) are almost temporally symmetric and relatively
32 long. The shallower portion of the source fault significantly contributes to the velocity and
33 displacement waveforms at near-fault sites. On the contrary, the slip velocity functions at
34 deeper depths (>3 km) are temporally asymmetric and have a sharp peak. The simulation of

35 the ground motion evolution suggests that the lateral flow in the Aso Valley was primarily
36 triggered by the strong forward-directivity pulse generated from the asperity on the Futagawa
37 fault.
38

39 INTRODUCTION

40 The M_{JMA} 7.3 mainshock of the 2016 Kumamoto earthquake sequence occurred in the
41 Kumamoto Prefecture, central Kyushu, Japan (Figure 1) at 01:25 Japan Standard Time (JST;
42 UTC+09:00) on April 16, 2016, ~28 h after the first M_{JMA} 6.5 earthquake on April 14, 2016. It
43 was a crustal earthquake that occurred along major active faults of the Futagawa and Hinagu
44 fault systems (e.g., Kumahara *et al.*, 2016; Shirahama *et al.*, 2016), which are developed in
45 areas with high inelastic strain rates in the center of Kyushu Island (Matsumoto *et al.*, 2016).
46 This right-lateral strike-slip earthquake had a normal-slip component, which is thought to be
47 due to lateral heterogeneous and depth-dependent stress fields (Matsumoto *et al.*, 2018).
48 Surface ruptures associated with this earthquake were widely observed in the area from the
49 Kumamoto Plain to the Aso caldera. Shirahama *et al.* (2016) surveyed surface ruptures in the
50 entire area and reported that they occurred along ~34 km of the Futagawa fault and the
51 northernmost portion of the Hinagu fault (northern part of the Takano–Shirahata segment).
52 They also reported a large slip, with a maximum dextral slip of 2.2 m, in the central section of
53 the rupture zone along the Futagawa fault and that the surface rupture along the Futagawa fault
54 extended to the western rim of the Aso caldera.

55 The ground motions during the 2016 Kumamoto earthquake were recorded by nationwide
56 strong motion networks (e.g., Suzuki *et al.*, 2017) as well as local observation networks of
57 seismic intensity (Japan Meteorological Agency, 2018). Suzuki *et al.* (2017) summarized the

58 features observed in strong motion records from strong motion networks K-NET and KiK-net
59 of the National Research Institute of Earth Science and Disaster Resilience (NIED) and
60 reported that large peak ground accelerations and velocities extended northeastward from the
61 epicentral area. Near-fault ground motions observed at several strong motion stations along the
62 Futagawa and Hinagu faults have received attention by seismological and engineering
63 communities (e.g., Furumura, 2016; Iwata and Asano, 2016; Kobayashi *et al.*, 2017; Ikutama
64 *et al.*, 2018; Kidoh and Nagano, 2020). Many studies have been conducted to investigate the
65 physical causes of extremely strong ground motions and building damage distribution
66 considering the effects of shallow soft sedimentary layers using aftershock and microtremor
67 observations in the damaged area (e.g., Yamanaka *et al.*, 2016; Kawase *et al.*, 2017; Yamada *et*
68 *al.*, 2017; Sun *et al.*, 2020).

69 Regarding the source effects, Asano and Iwata (2016) estimated a source rupture model for
70 the mainshock by the kinematic inversion of waveform data at 15 strong motion stations. They
71 revealed that the rupture started in the deep portion of a northwest-dipping fault in the northern
72 part of the Hinagu fault and propagated beyond the junction to the Futagawa fault. Most of the
73 significant slips (up to 5.1 m) occurred on the Futagawa fault. The source rupture process has
74 also been estimated in several other studies using kinematic waveform inversion of strong
75 motion data (Kubo *et al.*, 2016; Uchide *et al.*, 2016; Nozu and Nagasaka, 2017; Yoshida *et al.*,
76 2017; Hallo and Gallovič, 2020). The number of assumed fault segments varied from one to

77 four, except for Kubo *et al.* (2016) who used a curved fault model. Somei *et al.* (2020) modeled
78 three strong motion generation areas to simulate broadband strong ground motions in 0.2–10
79 Hz. Yagi *et al.* (2016) analyzed teleseismic P-wave data to estimate the rupture process of a
80 single fault plane along the Futagawa fault. Hao *et al.* (2017) jointly analyzed teleseismic and
81 strong motion displacement waveform data to estimate the kinematic rupture process of two
82 fault planes corresponding to the Futagawa and Hinagu faults. Fukahata and Hashimoto (2016)
83 and Himematsu and Furuya (2016) obtained slip models based on the geodetic inversion of
84 interferometric synthetic aperture radar (InSAR) data. Fukahata and Hashimoto (2016)
85 assumed two fault planes along the Futagawa and Hinagu faults and detected the largest slip of
86 >5 m with a significant normal-slip component close to the center of the Futagawa fault
87 (130.9°E). Himematsu and Furuya (2016) established a fault model with three segments and
88 concluded that slip partitioning occurred in an oblique extensional stress regime. Ozawa *et al.*
89 (2016) estimated four rectangular faults to explain InSAR and Global Navigation Satellite
90 System (GNSS) data using a dislocation model. Two were subparallel faults along the
91 Futagawa fault, one was a right-lateral strike slip fault with a high dip angle, and the other one
92 included a large normal-slip component with a low dip angle. Zhang *et al.* (2018) analyzed
93 InSAR, Global Positioning System (GPS), and strong motion data by assuming three fault
94 segments and Yue *et al.* (2017) analyzed GPS, strong motion, InSAR, and surface offset data
95 to obtain the kinematic rupture process for three curved fault models. Kobayashi *et al.* (2017)

96 carried out the joint inversion of teleseismic, strong motion, and GNSS data assuming five fault
97 segments including two subparallel faults in the central part of the Futagawa fault. Published
98 source models commonly include nearly unilateral rupture propagation from the hypocenter
99 near the junction or bend of the Hinagu and Futagawa faults into the northeastern direction
100 along the Futagawa fault. With respect to the generation mechanism of near-fault strong ground
101 motions, Kobayashi *et al.* (2017) demonstrated that extreme pulse-like ground motion
102 waveforms at near-field stations are attributed to the upward rupture directivity, slip rate, and
103 nearly simultaneous slip of two subparallel faults. However, the highest frequency of their
104 waveform analysis was limited to 0.4 Hz. The target frequency range in such studies should be
105 extended to higher frequencies to discuss the correlation between the source description and
106 the resultant ground motions.

107 Some of the above-mentioned studies focused on the correlation between the source rupture
108 process and geothermal structure of the Aso volcano. It has been concluded that the rupture of
109 the mainshock was terminated by a material barrier with high temperature and low seismic
110 velocity, which might be related to the presence of partial melting (Ozawa *et al.*, 2016; Yagi *et*
111 *al.*, 2016; Yue *et al.*, 2017; Zhang *et al.*, 2018). Seismic velocity tomography (Shito *et al.*, 2017;
112 Zhao *et al.*, 2018; Aoyagi *et al.*, 2020), seismic attenuation tomography (Komatsu *et al.*, 2017;
113 Wang *et al.*, 2017), and electrical resistivity structure surveys (Aizawa *et al.*, 2021) have been
114 conducted to quantitatively determine the correlation between the heterogeneous earthquake

115 source process and crustal structure. Information about this correlation is important for future
116 seismic hazard assessments because it could reduce the diversity in the source rupture scenarios,
117 which largely affects the ground motion prediction, and thus lead to more seismologically
118 reasonable ground motion predictions and seismic hazard assessments.

119 In this study, we used kinematic waveform inversion to reveal the fault rupture process of the
120 mainshock of the 2016 Kumamoto earthquake sequence. The multiple time-window linear
121 waveform inversion method (e.g., Hartzell and Heaton, 1983) was used to estimate the
122 kinematic rupture process, which was also employed in Asano and Iwata (2016). Based on this
123 method, the fault is divided into several subfaults and the point source is assumed to be in the
124 center of each subfault. The subfault dimensions are defined after considering the spatial
125 resolution of the data (e.g., Ammon *et al.*, 2020). However, the point sources should be densely
126 distributed across the fault plane to accurately reproduce the finite source effects in the near-
127 fault area because near-fault ground motion is quite sensitive to the discretization of the source
128 fault (e.g., Hisada and Bielak, 2003; Kidoh *et al.*, 2020; Wu *et al.*, 2021). The above-mentioned
129 papers suggest that the subfault size or point-source interval should be as small as 0.5 times the
130 fault distance to simulate accurately near-fault ground motions. On the other hand, the subfault
131 size used in Asano and Iwata (2016) was 2.0 km and the top depth of the source fault model
132 was about 2 km, and such setting was not necessarily efficient to reproduce ground motion
133 including permanent offset in the area very close to the surface ruptures. Therefore, we tried to

134 improve the representation of the source fault model in this study.

135 The improvement on that point is also required for quantitatively discussing the shape
136 and duration of slip velocity time function because the moment-rate function with a coarse
137 subfault size (2.0 km both in length and width) obtained in Asano and Iwata (2016) is a
138 convolution of local slip-velocity function and rupture propagation effect within the finite-sized
139 subfault. The shallowest discretized point-source in Asano and Iwata (2016) was located at
140 about 2.9 km depth. Therefore, it was not easy to discuss about depth-dependency of slip
141 velocity function directly from the obtained subfault moment-rate functions across the source
142 fault because long duration of the moment-rate function could also be explained to some extent
143 by long rupture duration. The characteristics of the slip velocity function can be analyzed in-
144 depth by setting dense distribution of element point-sources in the kinematic inversion scheme,
145 but it is necessary to avoid handling of an excessively large number of unknown parameters.
146 Thus, we propose an improved representation of the source fault model, which is suitable for
147 the reproduction of near-fault ground motions, and we also used the latest velocity structure
148 models in the target region, which was not available in 2016. The source fault planes were
149 extended to near the ground surface considering the geometry based on the latest study of the
150 aftershock distribution and the surface rupture distribution. The target frequency range was also
151 extended to higher frequencies than used in our previous work because the absolute amount of
152 slip-velocity function would also be affected by the width of the analyzed frequency range. Of

153 course, we expected that the general feature of the source process such as the location of large
154 slips will not change significantly because the original result was appropriately constrained by
155 many stations distributed in wide area.

156 The main focus of this study was placed on the depth dependency of the slip velocity
157 function of the source fault and its correlation with the crustal structure. The spatial relationship
158 between the whole rupture process and the known crustal structure or tectonic settings were
159 also addressed. Such studies may help to define the rupture area and the rupture scenario for
160 the seismic hazard modeling in advance. In addition, the forward-directivity pulse originating
161 from the heterogeneous source process of this earthquake and its contribution to the lateral flow
162 widely observed in the Aso Valley was discussed based on the estimated kinematic source
163 model and simulated ground motions.

164

165 **KINEMATIC WAVEFORM INVERSION AND FAULT PLANE MODEL**

166 Wald and Heaton (1994) proposed a method based on which the Green's function of the
167 subfault was obtained by summing up the responses of many point sources that were uniformly
168 distributed across the subfault to consider rupture front propagation within the subfault. Their
169 method requires the summation of Green's functions of individual point sources within a
170 subfault with appropriate rupture time delays based on the assumption of the velocity and
171 direction of the rupture front propagation in advance of starting the source inversion analysis.

172 Sekiguchi *et al.* (2002) alternatively proposed a convolution method in which a function
173 representing a bi-directional moving dislocation on each subfault was convolved with the
174 point-source synthetic wave from each subfault center.

175 In this study, we employed a slightly different approach. A schematic illustration of the
176 source fault representation is shown in Figure 2. Point sources were densely distributed across
177 the assumed fault planes, at intervals of 0.22 km. The relationship between the point-source
178 slip vector \mathbf{m}_p and data vector \mathbf{d} can be expressed as follows:

$$179 \quad \mathbf{d} = \mathbf{G}\mathbf{m}_p, \quad (1)$$

180 where the matrix \mathbf{G} contains the Green's functions from all point sources to the stations.
181 Unknown model parameters (slips in two orthogonal directions in each time window) were
182 assigned only to control points (larger circles in Figure 2) on the fault planes distributed at
183 intervals of 2.0 km in the strike and dip directions to avoid the introduction of excessive
184 complexity to the inverted source model. The slip of each individual point source in each time
185 window was then obtained by spatial bilinear interpolation of the slip amounts at the control
186 points. For example, the slip amount $m_{jk}(x, y)$ in the k -th direction in the j -th time window
187 of a point source located at (x, y) on a fault is given by the slip amounts of the four
188 surrounding control points (x_1, y_1) , (x_1, y_2) , (x_2, y_1) , and (x_2, y_2) :

$$m_{jk}(x, y) = (1 - a)(1 - b)m_{jk}(x_1, y_1) + (1 - a)bm_{jk}(x_1, y_2) + a(1 - b)m_{jk}(x_2, y_1) + abm_{jk}(x_2, y_2),$$

189

$$a = \frac{x - x_1}{x_2 - x_1},$$

$$b = \frac{y - y_1}{y_2 - y_1}, \quad (2)$$

190 where x and y are coordinates along the strike and dip directions of the fault, respectively. Thus,

191 \mathbf{m}_P can be linearly expressed with a model parameter vector \mathbf{m}_C and matrix \mathbf{A} containing

192 the coefficients required for spatial interpolation shown in Eq. (2).

$$193 \quad \mathbf{m}_P = \mathbf{A}\mathbf{m}_C. \quad (3)$$

194 The observation Eq. (1) becomes:

$$195 \quad \mathbf{d} = \mathbf{G}\mathbf{A}\mathbf{m}_C. \quad (4)$$

196 Therefore, the total number of unknown model parameters, which is the size of \mathbf{m}_C , is the

197 same as that of conventional kinematic source inversions and overparameterization can be

198 avoided.

199 We referred to the fault geometry models proposed by Mitsuoka *et al.* (2020) to set up the

200 fault plane model for the waveform inversion. They located hypocenters from 1993 to 2017

201 using permanent and temporary seismic stations in central Kyushu and derived the fault

202 geometry from the spatial distribution of the aftershocks. The fault plane model in our inversion

203 analysis was slightly modified to be consistent with surface rupture traces. It was composed of

204 five planar rectangular fault planes (Figure 1, Table 1). The surface projection of the fault

205 models is plotted with the aftershocks within 6 hours located by Mitsuoka *et al.* (2020) and the

206 surface rupture distribution compiled by Kumahara *et al.* (2016) in Figure 3a. Most aftershocks
207 in this period distributed in the depth range from 3 km to 18 km. Faults H1 and H2 have the
208 same strike angle but different dip angles. Fault H1 corresponds to the deeper portion of the
209 Hinagu fault and fault H2 is a vertical fault segment corresponding to the shallower portion of
210 the Hinagu fault as illustrated in Figure 3b. The aftershocks along the Hinagu Fault (H1 and
211 H2) did not distribute to the east of the Hinagu fault, therefore, we decided to assume that the
212 dip angle is nearly vertical in the shallow part of the Hinagu fault (H2). Faults F1, F2, and F3
213 are located along the Futagawa fault, and they are dipping northwestward in accordance with
214 the aftershock distribution in Figure 3c.

215 The rupture starting point was fixed at the hypocenter (32.758179°N, 130.766740°E,
216 12.808 km depth) reported by Mitsuoka *et al.* (2020) and was assumed to be on fault H1. The
217 total length of the assumed fault model was 44 km. All fault parameters are summarized in
218 Table 1. The total numbers of control points and point sources were 220 and 17,028,
219 respectively. The number of time windows was nine. The basis function of each time window
220 was a smoothed ramp function with a rise time of 1.0 s and each successive time window was
221 shifted by 0.5 s in the time domain. The slip direction at each control point was limited to -142°
222 $\pm 45^\circ$ using the non-negative least squares method (Lawson and Hanson, 1974). The rupture-
223 front propagation velocity triggering the first time-window was searched between 2.0 km/s and
224 3.0 km/s, and found a velocity giving the minimum residual among them. Spatiotemporal

225 smoothing constraint equations were introduced following Sekiguchi *et al.* (2000). The
226 appropriate weight of the smoothing constraints with respect to the observation equation was
227 determined by minimizing the Akaike Bayesian Information Criteria (ABIC, Akaike 1980).

228

229 **WAVEFORM DATA AND GREEN'S FUNCTIONS**

230 Strong ground motion waveform data around the source region were collected from the K-
231 NET, KiK-net, and F-net of NIED (Aoi *et al.*, 2020; NIED, 2019a, b), JMA earthquake
232 observation network, and seismic intensity observation network of the Kumamoto prefectural
233 government (Japan Meteorological Agency, 2018). Three-components of velocity waveforms
234 in a 30-s window starting 1 s before the S-wave onset at twenty strong motion stations were
235 used in this study (Figure 1). We used the records from the downhole sensors of the NIED KiK-
236 net stations and the records on the ground surface of other stations. Original acceleration
237 waveform data were integrated into velocity in the time domain, except for stations belonging
238 to NIED F-net, which was equipped with velocity-type strong motion sensors (TOKYO KEIKI
239 TSM-1). All velocity waveforms were bandpass-filtered between 0.05 and 1 Hz using the
240 Chebyshev filter and then resampled at 5 Hz.

241 The theoretical Green's function from each point source to a strong motion station was
242 calculated using the discrete wavenumber method (Bouchon, 1981) and reflection and
243 transmission matrix method (Kennett and Kerry, 1979). A station-dependent layer-cake model

244 was assumed for each station to consider local site amplification effects of the sedimentary
245 layers (e.g., Asano and Iwata, 2009). These one-dimensional velocity structure models were
246 extracted from the latest three-dimensional velocity structure models of the target region. The
247 velocity model for the sedimentary layers was based on three-dimensional models recently
248 developed by Senna *et al.* (2018) and Asano *et al.* (2019). Senna *et al.* (2018) constructed a
249 three-dimensional velocity model for the Kumamoto Plain and surroundings using phase
250 velocity dispersion curves and H/V spectra from microtremor observations, boring logs, and
251 gravity data. Asano *et al.* (2019) constructed a three-dimensional velocity model covering the
252 Yatsushiro Plain, Tamana Plain, Amakusa Islands, and other areas in the Kumamoto Prefecture
253 using P-wave reflection surveys, phase velocity dispersion curves and H/V spectra from
254 microtremor observations, boring logs, and gravity data. Because these velocity models were
255 developed above the seismic bedrock (S-wave velocity 3.1 km/s), we referred to the Japan
256 Integrated Velocity Structure Model Version 1 (JIVSM, Koketsu *et al.*, 2012) for the crust and
257 upper mantle structures. Thus, the velocity model used to calculate the Green's function
258 differed from that used in Asano and Iwata (2016). The lowest S-wave velocity of the velocity
259 model in the present study is 0.1 km/s, which corresponds to alluvial deposits in Quaternary
260 sedimentary plains. The S-wave velocity of the topmost layer at each station varies from 0.10
261 km/s to 0.35 km/s. The velocity models assigned to each station are summarized in the
262 Electronic Supplement (Tables S1–S20, available in the supplemental material to this article).

263 The theoretical Green's functions were bandpass-filtered and resampled with the same
264 procedure as that used for the observed waveforms.

265

266 **RESULTS**

267 The final slip distribution including slip vectors is shown in Figure 4a. The propagation
268 velocity of the first time-window front of this model is 2.4 km/s, yielding the minimum residual.
269 The average and maximum slip amounts over the entire fault are 1.9 and 4.9 m, respectively.
270 The slip velocity functions estimated for each control point are shown in Figure 4b and the
271 maximum peak slip velocity is 3.1 m/s. The characteristics of the slip velocity functions of the
272 faults are discussed in the following section. The total seismic moment is 4.89×10^{19} Nm (M_W
273 7.06). The fitting results for the waveforms, which are satisfactory for most stations, are shown
274 in Figure 5.

275 The overall slip distribution on the fault is similar to that of our previous model (Asano and
276 Iwata, 2016). The slip amount in the vicinity of the hypocenter of the mainshock is relatively
277 small, which indicates that the rupture started with a small initial rupture and intensified after
278 propagating along the Futagawa fault. The temporal rupture evolution presented in Figure 6
279 shows that the rupture of the Futagawa fault started after ~ 3 s in the deep portion of the fault
280 and propagated up- and northeastward. The slip in the shallow portion of the fault was delayed
281 compared with the deeper portion but not isolated. A large slip of 4–5 m was observed in the

282 depth range from ~3 to 15 km in the central part of the Futagawa fault. This large-slip area or
283 asperity has significant normal-slip components and a high slip velocity of 2–3 m/s. The
284 shallower part of the fault segments inside the western part of the Aso caldera also has a
285 relatively large normal slip (Figure 7) and it is consistent with surface displacements identified
286 during field surveys (e.g., Shirahama *et al.*, 2016; Toda *et al.*, 2019) and by satellite-based
287 geodetic measurements (e.g., Fujiwara *et al.*, 2016; Fukahata and Hashimoto, 2016;
288 Himematsu and Furuya, 2016; Ozawa *et al.*, 2016).

289 The slip of the Hinagu fault segments is nearly pure right-lateral strike-slip. The slip of the
290 Hinagu fault segments is concentrated in the northeastern part of the vertical fault segment,
291 which is consistent with the field observation of the surface rupture distribution along the
292 Hinagu fault (e.g., Shirahama *et al.*, 2016). The Hinagu fault also ruptured during the first
293 foreshock on April 14, 2016. Asano and Iwata (2016) established a slip model for this foreshock,
294 but the slips in the shallow portion of the foreshock and mainshock look complementary to
295 each other.

296

297 **DISCUSSIONS**

298 **Spatial variation of the source rupture characteristics and crustal structure**

299 The slip velocity on the fault is one of the key physical quantities controlling the generation
300 of a strong ground motion pulse (e.g., Miyake *et al.*, 2003; Gombert *et al.*, 2019; Wang *et al.*,

2019). As briefly mentioned in the introduction, strong ground motion pulses and permanent displacements at near-fault sites during the mainshock of the 2016 Kumamoto earthquake sequence have been modeled in many studies (e.g., Kobayashi *et al.*, 2017; Ikutama *et al.*, 2018; Tanaka *et al.*, 2018; Irikura *et al.*, 2020; Kidoh and Nagano, 2020). Kobayashi *et al.* (2017) explained near-fault ground motions by combining the effect of the up-dip rupture direction with the high slip velocity. Ikutama *et al.* (2018) proposed an approach based on which the entire ruptured fault from the ground surface to the bottom of the fault was modeled to reproduce strong ground motions and permanent displacements at sites close to the surface fault trace. In their approach, the asperity also extends to the near-surface layer and the source parameters of the entire fault follow the strong motion prediction recipe by Irikura and Miyake (2011). Tanaka *et al.* (2018) proposed the use of regularized Yoffe-type slip velocity functions in the shallower region (<3 km) above the seismogenic layer to evaluate long-period ground motions with permanent displacements in the near-fault region. However, the asperity extends into the shallow and seismogenic layers with a constant slip amount, similar to that reported by Ikutama *et al.* (2018). Irikura *et al.* (2020) proposed an extreme source model in which the rectangular area, that is, the long-period motion generation area (LMGA), is distributed in the shallow depth range above the seismogenic layer. However, the physical meaning of the LMGA remains unclear and its location and size depend on the availability of near-fault strong motion stations. Our final slip model (Figure 4a) does not indicate any isolated slip patch in the

320 shallower depth range, but it seems reasonable to consider the slips at shallow depths as spatial
321 extensions of the large fault slip in the seismogenic depth.

322 The slip velocity functions estimated for the control points of the Futagawa fault segments
323 are plotted in Figure 8. All control points belonging to one depth bin were plotted together in
324 one panel. Because the peak time of the slip velocity varies among subfaults due to the variation
325 in the rupture time, the slip velocity functions of each bin are aligned by the peak time. The
326 shapes of the slip velocity functions in the first two depth bins (depth <3 km) are almost
327 temporally symmetric and resemble the temporal derivative of a ramp function. The duration
328 is also relatively long compared with that of deeper depth bins. The peak time relative to the
329 onset time is distributed around 2 s for the shallow two depth bins. The average peak time
330 weighted by the peak slip velocity is 2.0 s for the depth bin of 0.3–0.5 km and 1.3 s for the
331 depth bin of 2.2–2.4 km. There are some subfaults where the peak time of slip velocity is
332 relatively faster than others, which might reflect spatial variation in material and frictional
333 parameters in this depth range. Larger slip-weakening distance (D_C) and small strength excess
334 in the shallow layer zone are possible factor making the slip-velocity function smooth and long
335 (e.g., Dalguer *et al.*, 2020). The free surface effect will also take additional role in generating
336 long rise time (e.g., Wang and Day, 2020). On the other hand, the slip velocity functions of the
337 rest of the eight depth bins, which are thought to be within the typical depth of the seismogenic
338 layer of Japanese crustal earthquakes, are temporally asymmetric and have a sharp peak. They

339 are similar to the Kostrov-type slip velocity function, which is typically expected based on
340 dynamic fault rupture modeling. The weighted average peak time is 0.7–1.0 s, and the majority
341 of the subfaults with large peak slip velocity have peak time of approximately 0.5 s. It could
342 also be noted that some subfaults in the westernmost part of the Futagawa fault, where slip
343 amount is relatively less, tend to have symmetric slip velocity function with long duration
344 (Figures 3 and 8), suggesting existence of crustal heterogeneity in the seismogenic zone and its
345 relationship to the rupture process. We think the depth-variable shape/duration of slip velocity
346 function should be considered for source model setting in future strong motion prediction or
347 earthquake hazard analysis of inland active faults because assumption of slip-velocity functions
348 in shallower portion of the fault would strongly affect simulated ground motions in earthquake
349 hazard modeling.

350 Figure 9 shows the comparison between the observed and synthetic velocity and
351 displacement waveforms at three near-fault strong motion stations. Stations 93011 and 93048
352 were used for the kinematic source inversion, but station 93051 was excluded from the source
353 inversion analysis because a borehole station of KiK-net KMMH16 was located 660 m
354 northeast of this station, which is preferable to use for avoiding any possibility of nonlinear
355 response. Our present simulation does not include any effect of nonlinear site response, which
356 is also important for analyzing large ground motions. The locations of these stations are shown
357 in Figure 7. One-dimensional velocity models for those stations are given in Tables S13, S14,

358 and S21 in the supplemental material to this article. The permanent displacement of the
359 synthetic waveforms reproduce well the observed displacements. To compare the contributions
360 of shallower and deeper parts of the fault rupture, the synthetic ground motions were separately
361 calculated for the shallower and deeper parts of the fault and plotted in this figure. The
362 shallower part corresponds to 13 point-sources (i.e., ~3 km depth) along the dip direction from
363 the top of the fault plane and the deeper part corresponds to the rest of the fault plane. The
364 velocity pulse and permanent displacement at stations 93048 and 93051 are mostly generated
365 in the shallower part of the fault, which is consistent with previous work by Kobayashi *et al.*
366 (2017). Contribution of the deeper portion is relatively large in the fault-normal component.
367 The forward-directivity pulse generated in the deeper portion of the fault significantly
368 contributes to the velocity waveforms at another station (93011) located in the direction of the
369 forward rupture propagation, and its contribution is comparable to that of the shallower portion
370 as seen in the velocity waveforms, which has comparable peak amplitude between fault-parallel
371 and fault-normal components.

372 It is quite important to investigate relationships between rupture process and crustal
373 structure in-depth. The rupture progression and slip-velocity function could be controlled by
374 the nature of seismogenic layer such as material heterogeneity, temperature, strength, frictional
375 parameters etc. For example, Shito *et al.* (2017) demonstrated seismic velocity tomography in
376 the source region using travel time data of many small events recorded at permanent and

377 temporary seismic stations. They found that low V_P (~ 5.0 km/s), low V_S (~ 2.5 km/s), and high
378 V_P/V_S (~ 1.9) were widely distributed at shallow depths (0.0–2.5 km). The upper depth limit of
379 the aftershock hypocenters was ~ 3 km. Thus, the boundary between the surface low-velocity
380 layer and the seismogenic layer ($V_P \sim 6.0$ km/s, $V_S \sim 3.5$ km/s) will be at ~ 3 km in this area.
381 Such structural difference might make difference in dynamic source parameters between the
382 surface low-velocity layer and the seismogenic layer.

383 Shito *et al.* (2017) also suggested that the high seismic velocity at a depth ranging from 5.0
384 to 12.5 km along the source fault of the 2016 Kumamoto earthquake compared with the
385 surrounding area on Kyushu Island is associated with high crustal strength and thus is
386 indicative of regions that can sustain high tectonic stress. The depth range correlates with the
387 location of the large-slip area of the Futagawa fault. This depth range in the central part of the
388 Futagawa fault is also characterized by a high- Q_P and high- Q_S (low attenuation) zone, as
389 revealed by seismic attenuation tomography in Komatsu *et al.* (2017).

390 Aizawa *et al.* (2021) imaged the electrical resistivity structure around the source faults of
391 the 2016 Kumamoto earthquake sequence using broadband magnetotelluric data from 200 sites
392 and found that the rupture of the mainshock arrested along the western edge of a low-resistivity
393 zone with high-temperature magmatic fluids beneath the Aso volcano. Komatsu *et al.* (2017)
394 detected a low- Q_P and low- Q_S (high attenuation) zone beneath the Aso caldera, suggesting high
395 temperature in this region. Miyakawa *et al.* (2016) also reported that the magma reservoir and

396 rupture termination are correlated based on three-dimensional gravity modeling of the Aso
397 caldera area. The lack of large slips in the deep part of our source model within the caldera rim
398 agrees with their findings. Aizawa *et al.* (2021) also concluded that the southward rupture of
399 the mainshock along the Hinagu fault terminated along the northern edge of another low-
400 resistivity zone along the Hinagu fault. Their finding is also supported by Aoyagi *et al.* (2020)
401 who concluded that the southern termination of the mainshock rupture along the Hinagu fault
402 was caused by a barrier with high V_P/V_S , which corresponds to the existence of the Rokkoku
403 Tectonic Line (RTL) by the seismic velocity structure around the Hinagu fault. RTL is a
404 geologic boundary intruded by serpentine and it makes vertical offset in the seismogenic layer
405 (Yanagida, 1958; Aoyagi *et al.*, 2020). We also think that such crustal structure is a primary
406 factor for the fact that the rupture of the 2016 Kumamoto earthquake did not propagate
407 southwestward along the Hinagu fault. The electric conductivity can be used to image
408 heterogeneous source structures prior to future destructive earthquakes because it does not
409 require many aftershocks in the source region. The spatial relationship between the crustal
410 structure and slip heterogeneity must be understood to provide geophysical constraints for
411 scenario source models used for the strong motion prediction of future inland crustal
412 earthquakes.

413

414 **Lateral flow in the Aso caldera triggered by a forward-directivity pulse**

415 Another phenomenon observed for the 2016 Kumamoto earthquake is the emergence of
416 many open fissures and associated horizontal sliding of geologic blocks in the Aso Valley, the
417 northern part of the Aso Caldera. Fujiwara *et al.* (2017) reported large-scale surface
418 deformation in three areas with diameters of 500 m to 2 km in the Aso Valley, which is underlain
419 by thick lake-bottom deposits consisting of saturated silt. Each area was horizontally displaced
420 by more than 2 m in the north–northwest direction. Based on differential interferometric
421 synthetic aperture radar data, field observations, descriptions of the temporal and spatial
422 variations of the hot spring supplies, and data from a borehole camera, Tsuji *et al.* (2017)
423 suggested that the shallow geologic block of the Aso hot spring slid more than 1 m in the
424 northwest direction along a specific geologic layer at a depth of ~50 m.

425 Two strong motion stations (KMMH04 and 93002 in Figure 7) are located within the above-
426 mentioned displaced geological blocks. The distance between the two stations is 3.1 km. Figure
427 10 shows the velocity and displacement waveforms recorded at these two stations 30 s after
428 the rupture. The horizontal ground motion at station 93002 was rotated by 36° with respect to
429 the original records to correct for the misorientation of the sensor located inside a kitchenette
430 in the Uchinomaki branch of the Aso city office. The ground motions measured at these two
431 sites are similar. The ground displacement is characterized by a significant horizontal
432 permanent displacement toward the north to north–northwest direction and subsidence was not
433 observed. Such a displacement field cannot be explained by the fault movement of strike-slip

434 faults or normal faults striking in the northeast–southwest direction. Thus, it is reasonable to
435 interpret these displacements as lateral flow or horizontal sliding beneath those sites.

436 We simulated ground motions at those two stations using our source model and velocity
437 structure models in Tables S22 and S23 in the supplemental material to this article. The
438 simulation method is the discrete wavenumber method, which was also used in the waveform
439 inversion study. The simulated velocity waveforms derived from the estimated source model
440 show a strong forward-directivity pulse in the northwestward fault-normal direction as
441 demonstrated in Figure 10, which originated from the asperity in the central part of the
442 Futagawa fault. The synthetic and observed velocity waveforms match well before the peak
443 ground velocity is reached. After the forward-directivity pulse passed, the discrepancy between
444 the observed and synthetic waveforms became nonnegligible. The observed velocity
445 waveforms show a remarkably slow deceleration after the peak, which is particularly noticeable
446 in the north–south component. The waveform comparison suggests that this peculiar ground
447 motion might be due to a force applied to a superficial geological block during lateral flow.
448 There are thick low-velocity sediments in the Aso valley because caldera lakes existed for long
449 years in the Holocene and Pleistocene (e.g., Miyabuchi and Sugiyama, 2012). The current
450 velocity models for these two stations (Tables S22 and S23) include thick low-velocity
451 sediments based on the subsurface structure model by Senna *et al.* (2018), thus, the synthetic
452 waveforms were affected by these lakebed sediments as basin-induced surface waves. However,

453 such phenomena were not recorded in the observed waveforms because the horizontal sliding
454 by liquefaction at a shallow depth (e.g., Tsuji *et al.*, 2017) might not allow seismic waves
455 propagate from deep valley to the surface, and the seismometer moved with the sliding block.
456 Unfortunately, the downhole record of KMMH04 at a depth of 127 m, which is much deeper
457 than the expected bottom depth of the displaced block, could not be used because the downhole
458 sensor was out of order at the time of the earthquake. Therefore, we could not directly observe
459 the relative movement between the surface and downhole records. Our source model and the
460 ground motion simulation enabled us to provide evidence that the lateral flow in the Aso Valley
461 area was primarily dynamically triggered by the northwest motion of the forward-directivity
462 pulse, which is preponderance in the fault-normal component over the fault-parallel component.
463 The same forward-directivity pulse might also have contributed to the remote triggering of a
464 M 5.9 event in the Yufuin geothermal area (e.g., Miyazawa, 2016).

465

466 **CONCLUSIONS**

467 In this study, an improved approach is proposed for the parameterization of the source fault
468 during kinematic waveform inversion analysis to enhance the reproducibility of the near-fault
469 ground motions during the mainshock of the 2016 Kumamoto earthquake sequence, central
470 Kyushu, Japan (M_{JMA} 7.3). Point sources, which were densely distributed at intervals of 0.22
471 km, were utilized in this work. The slip amount of each point source was obtained via the linear

472 correlation with the slip amounts at surrounding control points, which were uniformly
473 distributed across the source fault, at intervals of 2.0 km. A source fault plane model consisting
474 of five fault segments was set up using fault geometries recently proposed by Mitsuoka *et al.*
475 (2020) based on the distribution of aftershocks. The estimated source rupture process started
476 with a small initial rupture in the vicinity of the hypocenter of the Hinagu fault within the first
477 three seconds. The rupture then propagated up- and northeastward along the Futagawa fault. A
478 large slip with a peak of 4.9 m and peak slip-velocity of 3.1 m/s was detected at depths ranging
479 from 3 to 15 km in the central part of the Futagawa fault, which could be characterized as a
480 body with high seismic velocity and low seismic attenuation from published seismic velocity
481 and attenuation tomography studies. The slips in the shallower portion of the fault were not
482 isolated and can be regarded as extensions of the asperity into the seismogenic depth, but the
483 rupture was delayed compared with the slips in the deeper portion. The slip in the Aso caldera
484 is concentrated at shallow depth, which is consistent with surface ruptures, geodetically
485 measured displacement fields, and the existence of high-temperature magma fluid beneath the
486 Aso volcano. The slip velocity functions show depth-dependent features. The slip velocity
487 functions at the top 3 km are almost temporally symmetric and have relatively long durations
488 (4–5 s), although the slip velocity functions of the rest of the fault plane (>3 km depth) inside
489 the seismogenic layer have typical Kostrov-type characteristics with short durations. The slips
490 and slip velocities in the shallow portion of the source fault significantly contributed to the

491 pulse wave velocity and permanent displacement, except for sites located in the forward-
492 rupture direction.

493 Geophysical information on the crustal structure would be beneficial for the characterization
494 of the behaviors of source fault ruptures and is necessary for advancing source models used for
495 scenario-based strong motion prediction and seismic hazard assessment. Based on our results,
496 lateral flow of superficial layers observed in wide areas of the Aso Valley, northern Aso caldera,
497 was primarily triggered by the northwestward ground motion of a strong forward-directivity
498 pulse generated by the asperity on the Futagawa fault.

499

500 **DATA AND RESOURCES**

501 Strong motion data of K-NET and KiK-net were downloaded from the strong-motion
502 seismograph network (<https://www.kyoshin.bosai.go.jp/>, last accessed September 2016)
503 operated by the National Research Institute for Earth Science and Disaster Resilience (NIED),
504 Japan. The strong motion waveform data of F-net were downloaded from the NIED Hi-net
505 database (<https://www.hinet.bosai.go.jp/>, last accessed April 2016). The strong motion data
506 from the seismic intensity observation networks of the JMA and Kumamoto prefectural
507 government were obtained from JMA's website
508 (http://www.data.jma.go.jp/svd/eqev/data/kyoshin/jishin/1604160125_kumamoto/index.html,
509 last accessed July 2016). The 10 m-mesh digital elevation model used in the maps was provided

510 from the Geospatial Information Authority of Japan as the Fundamental Geospatial Data
511 (<https://www.gsi.go.jp/kiban/>). The supplemental material contains the 1D velocity structure
512 model of each strong motion station used for calculating Green's functions. All figures were
513 drawn using Generic Mapping Tools version 6 (Wessel *et al.*, 2019).

514

515 **DECLARATION OF COMPETING INTERESTS**

516 The authors acknowledge there are no conflicts of interest recorded.

517

518 **ACKNOWLEDGEMENTS**

519 This study was supported by the Earthquake and Volcano Hazards Observation and Research
520 Program of the Ministry of Education, Culture, Sports, Science and Technology (MEXT),
521 Japan. The authors are grateful for the careful and constructive reviews by Editor-in-Chief
522 Thomas L. Pratt, the guest editors of this special section, and two anonymous reviewers.

523

524 **References**

- 525 Aizawa, K., S. Takamura, H. Asaue, K. Koike, R. Yoshimura, K. Yamazaki, S. Komatsu, M.
526 Utugi, H. Inoue, K. Tsukamoto, M. Uyeshima, T. Koyama, W. Kanda, T. Yoshinaga, N.
527 Matsushima, K. Uchida, Y. Tsukashima, T. Matsushima, H. Ichihara, D. Muramatsu, Y.
528 Teguri, A. Shito, S. Matsumoto, and H. Shimizu (2021). Electrical conductive fluid-rich
529 zones and their influence on the earthquake initiation, growth, and arrest processes:
530 observations from the 2016 Kumamoto earthquake sequence, Kyushu Island, Japan, *Earth*
531 *Planets Space* **73**, 12, doi: 10.1186/s40623-020-01340-w.
- 532 Akaike, H. (1980). Likelihood and the Bayes procedure, *Trab. Estad. Invest. Oper.* **31**, no. 1,
533 143-166, doi: 10.1007/BF02888350.
- 534 Ammon, C. J., A. A. Velasco, T. Lay, and T. C. Wallace (2020). *Foundation of Modern Global*
535 *Seismology*, Second Ed., Academic Press, London, 531-535. doi: 10.1016/C2017-0-03756-
536 4.
- 537 Aoi, S., Y. Asano, T. Kunugi, T. Kimura, K. Uehira, N. Takahashi, H. Ueda, K. Shiomi, T.
538 Matsumoto, and H. Fujiwara (2020). MOWLAS: NIED observation network for earthquake,
539 tsunami and volcano, *Earth Planets Space* **72**, 126, doi: 10.1186/s40623-020-01250-x.
- 540 Aoyagi, Y., H. Kimura, and K. Mizoguchi (2020). Seismic velocity structure at the southern
541 termination of the 2016 Kumamoto Earthquake rupture, Japan, *Earth, Planets Space* **72**,
542 142, doi: 10.1186/s40623-020-01276-1.

543 Asano, K., and T. Iwata (2009). Source rupture process of the 2004 Chuetsu, Mid-Niigata
544 prefecture, Japan, earthquake inferred from waveform inversion with dense strong-motion
545 data, *Bull. Seism. Soc. Am.* **99**, no. 1, 123-140, doi: 10.1785/0120080257.

546 Asano, K., and T. Iwata (2016). Source rupture processes of the foreshock and mainshock in
547 the 2016 Kumamoto earthquake sequence estimated from the kinematic waveform
548 inversion of strong motion data, *Earth Planets Space* **68**, 147, doi:10.1186/s40623-016-
549 0519-9.

550 Asano, K., T. Iwata, M. Yoshimi, H. Miyake, H. Sekiguchi, S. Matsushima, H. Kawase, F.
551 Nagashima, H. Yamanaka, K. Chimoto, N. Yamada, T. Kanno, M. Shigefuji, S. Senna, T.
552 Maeda, A. Wakai, A. Iwaki, K. Jin, H. Saomoto, S. Tsuno, M. Korenaga, T. Sugiyama, H.
553 Suzuki, H. Matsuyama, J. Manabe, A. Yatagai, S. Okamoto, and M. Suehiro (2019). Strong
554 ground motion prediction for the source fault model of Futagawa and Hinagu active fault
555 zones (1) Construction of the basin velocity structure model, *Japan Geoscience Union*
556 *Meeting 2019*, Abstract SSS13-09.

557 Bouchon, M. (1981). A simple method to calculate Green's function for elastic layered media,
558 *Bull. Seismol. Soc. Am.* **71**, no. 4, 959-971.

559 Dalguer, L. A., H. Wu, Y. Matsumoto, K. Irikura, T. Takahama, and M. Tonagi (2020).
560 Development of dynamic asperity models to predict surface fault displacement caused by
561 earthquakes, *Pure Appl. Geophys.* **177**, no. 5, 1983-2006, doi: 10.1007/s00024-019-02255-

562 8.

563 Fujiwara, S., Y. Morishita, T. Nakano, T. Kobayashi, and H. Yurai (2017). Non-tectonic
564 liquefaction-induced large surface displacements in the Aso Valley, Japan, caused by the
565 2016 Kumamoto earthquake, revealed by ALOS-2 SAR, *Earth Planet. Sci. Lett.* **474**, 457-
566 465, doi: 10.1016/j.epsl.2017.07.001.

567 Fujiwara, S., H. Yurai, T. Kobayashi, Y. Morishita, T. Nakano, B. Miyahara, H. Nakai, Y. Miura,
568 H. Ueshiba, Y. Kakiage, and H. Une (2016). Small-displacement linear surface ruptures of
569 the 2016 Kumamoto earthquake sequence detected by ALOS-2 SAR interferometry, *Earth*
570 *Planets Space* **68**, 160, doi: 10.1186/s40623-016-0534-x.

571 Fukahata, Y., and M. Hashimoto (2016). Simultaneous estimation of the dip angles and slip
572 distribution on the faults of the 2016 Kumamoto earthquake through a weak nonlinear
573 inversion of InSAR data, *Earth Planets Space* **68**, 204, doi: 10.1186/s40623-016-0580-4.

574 Furumura, T. (2016). Destructive near-fault strong ground motion from the 2016 Kumamoto
575 prefecture, Japan, M7.3 earthquake, *Landslides* **13**, no. 6, 1519-1524, 10.1007/s10346-016-
576 0760-0.

577 Gombert, B., Z. Duputel, E. Shabani, L. Rivera, R. Jolivet, and J. Hollingsworth (2019).
578 Impulsive Source of the 2017 Mw 7.3 Ezgeleh, Iran, Earthquake, *Geophys. Res. Lett.* **46**,
579 no. 10, 5207-5216, doi: 10.1029/2018gl081794.

580 Hallo, M., and F. Gallovič (2020). Bayesian Self-Adapting Fault Slip Inversion with Green's

581 Functions Uncertainty and Application on the 2016 M_w 7.1 Kumamoto Earthquake, *J.*
582 *Geophys. Res. Solid Earth* **125**, no. 3, e2019JB018703, doi: 10.1029/2019JB018703.

583 Hao, J., C. Ji, and Z. Yao (2017). Slip history of the 2016 M_w 7.0 Kumamoto earthquake:
584 Intraplate rupture in complex tectonic environment, *Geophys. Res. Lett.* **44**, no. 2, 743-750,
585 doi: 10.1002/2016GL071543.

586 Hartzell, S.H., and Heaton (1983). Inversion of strong ground motion and teleseismic
587 waveform data for the fault rupture history of the 1979 Imperial Valley, California,
588 earthquake, *Bull. Seismol. Soc. Am.* **73**, no. 6, 1553-1583.

589 Himematsu, Y., and M. Furuya (2016). Fault source model for the 2016 Kumamoto earthquake
590 sequence based on ALOS-2/PALSAR-2 pixel-offset data: evidence for dynamic slip
591 partitioning, *Earth Planets Space* **68**, 169, doi: 10.1186/s40623-016-0545-7.

592 Hisada, Y., and Bielak (2003). A theoretical method for computing near-fault ground motions
593 in layered half-spaces considering static offset due to surface faulting, with a physical
594 interpretation of fling step and rupture directivity, *Bull. Seismol. Soc. Am.* **93**, no. 3, 1154-
595 1168, doi: 10.1785/0120020165.

596 Ikutama, S., T. Kawasato, Y. Kawakami, M. Noshi, A. Oana, K. Dan, H. Torita, and Y. Okada
597 (2018). Source modeling for predicting ground motions and permanent displacements very
598 close to the fault trace, *J. Earthq. Tsunami* **12**, no. 4, 1841005, doi:
599 10.1142/S1793431118410051.

600 Irikura, K., S. Kurahashi, and Y. Matsumoto (2020). Extension of characterized source model
601 for long-period ground motions in near-fault area, *Pure Appl. Geophys.* **177**, no. 5, 2021-
602 2047, doi: 10.1007/s00024-019-02283-4.

603 Irikura, K., and H. Miyake (2011). Recipe for predicting strong ground motion from crustal
604 earthquake scenarios, *Pure Appl. Geophys.* **168**, nos. 1-2, 85-104, doi: 10.1007/s00024-010-
605 0150-9.

606 Iwata, T., and K. Asano (2016). Near-fault strong ground motions during the 2016 Kumamoto,
607 Japan, earthquake, *Am. Geophys. Union, Fall Meeting 2016*, Abstract S53B-2867.

608 Japan Meteorological Agency (2018) Report of the 2016 Kumamoto earthquake by Japan
609 Meteorological Agency, *Tech. Rep. Japan Met. Ag.* **135**, 1-309. (in Japanese with English
610 abstract)

611 Kawase, H., S. Matsushima, F. Nagashima, and K. Nakano (2017). The cause of heavy damage
612 concentration in downtown Mashiki inferred from observed data and field survey of the
613 2016 Kumamoto earthquake sequence and its impact on earthquake, *Earth Planets Space*
614 **69**, 3, doi: 10.1186/s40623-016-0591-1.

615 Kennett, B., and N. J. Kerry (1979). Seismic waves in a stratified half space, *Geophys. J. R.*
616 *Astron. Soc.* **57**, no. 3, 557-583.

617 Kidoh, T., and M. Nagano (2020). Interpretation of large-amplitude velocity pulses during the
618 2016 Kumamoto earthquake and the effects of the shallow and deep parts of the fault

619 ruptures on the near-fault ground motions, *J. Struct. Constr. Eng., Trans. AIJ* **85**, no. 773,
620 879-889, doi: 10.3130/aijs.85.879. (in Japanese with English abstract)

621 Kidoh, T., Nagano, M., and Hikima (2020). Verification of theoretical evaluation of near-fault
622 seismic ground motions by difference of sub-faults division based on thin layer method, *J.*
623 *Jpn Assoc. Earthq. Eng* **20**, no. 1, 118-132, doi: 10.5610/jaee.20.1_118. (in Japanese with
624 English abstract)

625 Kobayashi, H., K. Koketsu, and H. Miyake (2017). Rupture processes of the 2016 Kumamoto
626 earthquake sequence: Causes for extreme ground motions, *Geophys. Res. Lett.* **44**, no. 12,
627 6002-6010, doi: 10.1002/2017GL073857.

628 Koketsu, K., H. Miyake, and H. Suzuki (2012). Japan Integrated Velocity Structure Model
629 Version 1, *Proc. 15th World Conf. Earthq.*, paper no. 1773.

630 Komatsu, M., H. Takenaka, and H. Oda (2017). Three-dimensional P- and S-wave attenuation
631 structures around the source region of the 2016 Kumamoto earthquakes, *Earth Planets*
632 *Space* **69**, 101, doi:10.1186/s40623-017-0683-6.

633 Kubo, H., W. Suzuki, S. Aoi, and H. Sekiguchi (2016). Source rupture processes of the 2016
634 Kumamoto, Japan, earthquakes estimated from strong-motion waveforms, *Earth Planets*
635 *Space*, **68**, 161, doi: 10.1186/s40623-016-0536-8.

636 Kumahara, Y., H. Goto, T. Nakata, S. Ishiguro, D. Ishimura, T. Ishiyama, S. Okada, K.
637 Kagohara, S. Kashihara, H. Kaneda, N. Sugito, Y. Suzuki, D. Takenami, K. Tanaka, T.

638 Tanaka, H. Tsutsumi, S. Toda, D. Hirouchi, N. Matsuta, T. Mita, H. Moriki, H. Yoshida, and
639 M. Watanabe (2016). Distribution of surface rupture associated the 2016 Kumamoto
640 earthquake and its significance, *Abstracts of Japan Geoscience Union Meeting 2016*,
641 MIS34-05.

642 Lawson, C. L., and R. J. Hanson (1974). *Solving Least Squares Problems*, Prentice-Hall, Old
643 Tappan.

644 Matsumoto, S., T. Nishimura, and T. Ohkura (2016) Inelastic strain rate in the seismogenic
645 layer of Kyushu Island, Japan, *Earth Planets Space*, **68**, 207, doi: 10.1186/s40623-016-
646 0584-0.

647 Matsumoto S., Y. Yamashita, M. Nakamoto, M. Miyazaki, S. Sakai, Y. Iio, H. Shimizu, K. Goto,
648 T. Okada, M. Ohzono, T. Terakawa, M. Kosuga, M. Yoshimi, and Y. Asano (2018). Prestate
649 of stress and fault behavior during the 2016 Kumamoto earthquake (M7.3), *Geophys. Res.*
650 *Lett.* **45**, no. 2, 637-645, doi: 10.1002/2017GL075725.

651 Mitsuoka, A., A. Shito, S. Matsumoto, Y. Yamashita, M. Nakamoto, S. Sakai, Y. Iio, H. Shimizu,
652 K. Goto, T. Okada, M. Ohzono, Y. Yamanaka, M. Kosuga, M. Yoshimi, and Y. Asano (2020).
653 Spatiotemporal change in the stress state around the hypocentral area of the 2016
654 Kumamoto earthquake sequence, *J. Geophys. Res. Solid Earth* **125**, no. 9, e2019JB018515,
655 doi: 10.1029/2019JB018515.

656 Miyabuchi, I., and S. Sugiyama (2012). Holocene vegetation history based on phytolith records

657 in Asodani Valley, northern part of the Aso Caldera, Japan, *Quat. Int.* **254**, 73-82, doi:
658 doi.org/10.1016/j.quaint.2011.09.024.

659 Miyakawa, A., T. Sumita, Y. Okubo, R. Okuwaki, M. Otsubo, S. Uesawa, and Y. Yagi (2016).
660 Volcanic magma reservoir imaged as a low-density body beneath Aso volcano that
661 terminated the 2016 Kumamoto earthquake rupture, *Earth Planets Space* **68**, 208, doi:
662 10.1186/s40623-016-0582-2.

663 Miyake, H., T. Iwata, and K. Irikura (2003). Source characterization for broadband ground-
664 motion simulation: Kinematic heterogeneous source model and strong motion generation
665 area, *Bull. Seismol. Soc. Am.* **93**, no. 6, 2531-2545, doi: 10.1785/0120020183.

666 Miyazawa, M. (2016). An investigation into the remote triggering of the Oita earthquake by
667 the 2016 Mw 7.0 Kumamoto earthquake using full wavefield simulation, *Earth Planets*
668 *Space* **68**, 205, doi: 10.1186/s40623-016-0585-z.

669 National Research Institute for Earth Science and Disaster Resilience (2019a). NIED K-NET,
670 KiK-net, National Research Institute for Earth Science and Disaster Resilience,
671 doi:10.17598/NIED.0004.

672 National Research Institute for Earth Science and Disaster Resilience (2019b). NIED F-net,
673 National Research Institute for Earth Science and Disaster Resilience,
674 doi:10.17598/NIED.0005.

675 Nozu, A., and Y. Nagasaka (2017). Rupture process of the main shock of the 2016 Kumamoto

676 earthquake with special reference to damaging ground motions: waveform inversion with
677 empirical Green's functions, *Earth Planets Space* **69**, 22, doi: 10.1186/s40623-017-0609-3.

678 Ozawa, T., E. Fujita, and H. Ueda (2016). Crustal deformation associated with the 2016
679 Kumamoto Earthquake and its effect on the magma system of Aso volcano, *Earth Planets*
680 *Space* **68**, 186, doi: 10.1186/s40623-016-0563-5.

681 Sekiguchi, H., K. Irikura, and T. Iwata (2002). Source inversion for estimating continuous slip
682 distribution on the fault - Introduction of Green's functions convolved with a correction
683 function to give moving dislocation effects in subfaults -, *Geophys. J. Int.* **150**, no. 2, 377-
684 391, doi: 10.1046/j.1365-246X.2002.01669.x.

685 Sekiguchi, H., T. Iwata, and K. Irikura (2000). Fault geometry at the rupture termination of the
686 1995 Hyogo-ken Nanbu earthquake, *Bull. Seismol. Soc. Am.* **90**, no. 1, 117-133.

687 Senna, S., A. Wakai, H. Suzuki, A. Yatagai, H. Matsuyama, and H. Fujiwara (2018). Modeling
688 of the subsurface structure from the seismic bedrock to the ground surface for a broadband
689 strong motion evaluation in Kumamoto Plain, *J. Disas. Res.* **13**, no. 5, 917-927, doi:
690 10.20965/jdr.2018.p0917.

691 Shirahama, Y., M. Yoshimi, Y. Awata, T. Maruyama, T. Azuma, Y. Miyashita, H. Mori, K.
692 Imanishi, N. Takeda, T. Ochi, M. Otsubo, D. Asahina, and A. Miyakawa (2016).
693 Characteristics of the surface ruptures associated with the 2016 Kumamoto earthquake
694 sequence, central Kyushu, Japan, *Earth Planets Space* **68**, 191, doi: 10.1186/s40623-016-

695 0559-1.

696 Shito, A., S. Matsumoto, H. Shimizu, T. Ohkura, H. Takahashi, S. Sakai, T. Okada, H.
697 Miyamachi, M. Kosuga, Y. Maeda, M. Yoshimi, Y. Asano, and M. Okubo (2017). Seismic
698 velocity structure in the source region of the 2016 Kumamoto earthquake sequence, Japan,
699 *Geophys. Res. Lett.* **44**, no. 15, 7766-7772.

700 Somei, K., K. Miyakoshi, K. Yoshida, S. Kurahashi, and K. Irikura (2020). Near-source strong
701 pulses during two large M_{JMA} 6.5 and M_{JMA} 7.3 events in the 2016 Kumamoto, Japan,
702 earthquakes, *Pure Appl. Geophys.* **177**, no. 5, 2223-2240, doi: 10.1007/s00024-019-02095-
703 6.

704 Sun, J., F. Nagashima, H. Kawase, and S. Matsushima (2020). Site effects analysis of shallow
705 subsurface structures at Mashiki Town, Kumamoto, based on microtremor horizontal-to-
706 vertical spectral ratios, *Bull. Seismol. Soc. Am.* **110**, no. 6, 2912-2938, doi:
707 10.1785/0120190318.

708 Suzuki, W., S. Aoi, T. Kunugi, H. Kubo, N. Morikawa, H. Nakamura, T. Kimura, and H.
709 Fujiwara (2017). Strong motions observed by K-NET and KiK-net during the 2016
710 Kumamoto earthquake sequence, *Earth Planets Space* **69**, 19, doi:10.1186/s40623-017-
711 0604-8.

712 Tanaka, S., J. Kaneda, K. Hikima, and Y. Hisada (2018). Characterized fault model for
713 prediction of long-period ground motions containing permanent displacement in the near-

714 fault region, *J. Struct. Constr. Eng. (Trans. AIJ)* **83**, no. 752, 1525-1535, doi:
715 10.3130/aajs.83.1525. (in Japanese with English abstract)

716 Toda, S., M. Torii, M. Okuno, A. Konno, H. Ono, and N. Takahashi (2019). Evidence for
717 Holocene paleoseismic events on the 2016 Kumamoto earthquake rupture zone within the
718 Aso caldera: A trench excavation survey at Kurokawa, the town of Minami-Aso, southwest
719 Japan, *Active Fault Res.* **51**, 13-25, doi: 10.11462/afr.2019.51_13. (in Japanese with English
720 abstract)

721 Tsuji T, J. Ishibashi, K. Ishitsuka, and R. Kamata (2017). Horizontal sliding of kilometre-scale
722 hot spring area during the 2016 Kumamoto earthquake, *Sci. Rep.* **7**, 42947, doi:
723 10.1038/srep42947.

724 Uchide, T., H. Horikawa, M. Nakai, T. Matsushita, M. Shigematsu, R. Ando, and K. Imanishi
725 (2016). The 2016 Kumamoto–Oita earthquake sequence: aftershock seismicity gap and
726 dynamic triggering in volcanic areas, *Earth Planets Space* **68**, 180, doi:10.1186/s40623-
727 016-0556-4.

728 Wald, D. J., and T. H. Heaton (1994). Spatial and temporal distribution of slip for the 1992
729 Landers, California, earthquake, *Bull. Seismol. Soc. Am.* **84**, no. 3, 668-691.

730 Wang, Y., and S. M. Day (2020). Effects of off-fault inelasticity on near-fault directivity pulses,
731 *J. Geophys. Res. Solid Earth* **125**, no. 7, e2019JB019074 , doi; 10.1029/2019JB019074.

732 Wang, Y., S. M. Day, and M. A. Denolle (2019). Geometric controls on pulse-like rupture in a

733 dynamic model of the 2015 Gorkha earthquake, *J. Geophys. Res. Solid Earth* **124**, no. 2,
734 1544-1568, doi: 10.1029/2018jb016602.

735 Wang, Z., D. Zhao, X. Liu, and X. Li (2017). Seismic attenuation tomography of the source
736 zone of the 2016 Kumamoto earthquake ($M 7.3$), *J. Geophys. Res. Solid Earth* **122**, no. 4,
737 2988-3007, doi: 10.1002/2016JB013704.

738 Wessel, P., J. F. Luis, L. Uieda, R. Scharroo, F. Wobbe, W. H. F. Smith, and D. Tian (2019).
739 Generic Mapping Tools Version 6, *Geochem. Geophys. Geosyst.* **20**, no. 11, 5556-5564.

740 Wu, S., A. Nozu, and Y. Nagasaka (2021) Accuracy of near-fault fling-step displacements
741 estimated using the discrete wavenumber method, *Bull. Seismol. Soc. Am.* **111**, no. 1, 309-
742 320, doi: 10.1785/0120190257.

743 Yagi, Y., R. Okuwaki, B. Enescu, A. Kasahara, A. Miyakawa, and M. Otsubo (2016). Rupture
744 process of the 2016 Kumamoto earthquake in relation to the thermal structure around Aso
745 volcano, *Earth Planet Space* **68**, 118, doi: 10.1186/s40623-016-0492-3.

746 Yamada, M., J. Ohmura, and H. Goto (2017). Wooden building damage analysis in Mashiki
747 Town for the 2016 Kumamoto earthquakes on April 14 and 16, *Earthq. Spectra* **33**, no. 4,
748 1555-1572, doi: 10.1193/090816EQS144M.

749 Yamanaka, H., K. Chimoto, H. Miyake, S. Tsuno, and N. Yamada (2016). Observation of
750 earthquake ground motion due to aftershocks of the 2016 Kumamoto earthquake in
751 damaged areas, *Earth Planets Space* **68**, 197, doi: 10.1186/s40623-016-0574-2.

752 Yanagida, J. (1958). The Upper Permian Mizukoshi Formation, *J. Geol. Soc. Jpn.* **64**, 222-231,
753 doi: 10.5575/geosoc.64.222. (in Japanese with English abstract)

754 Yoshida, K., K. Miyakoshi, K. Somei, and K. Irikura (2017). Source process of the 2016
755 Kumamoto earthquake (Mj7.3) inferred from kinematic inversion of strong-motion records,
756 *Earth Planets Space* **69**, 64, doi: 10.1186/s40623-017-0649-8.

757 Yue, H., Z. E. Ross, C. Liang, S. Michel, H. Fattahi, E. Fielding, A. Moore, Z. Liu, and B. Jia
758 (2017). The 2016 Kumamoto $M_w = 7.0$ earthquake: A significant event in a fault-volcano
759 system, *J. Geophys. Res. Solid Earth* **122**, no. 11, 9166-9183, doi: 10.1002/2017JB014525.

760 Zhang, Y., X. Shan, G. Zhang, W. Gong, X. Liu, H. Yin, D. Zhao, S. Wen, and C. Qu (2018).
761 Source model of the 2016 Kumamoto, Japan, earthquake constrained by InSAR, GPS, and
762 strong-motion data: Fault slip under extensional stress, *Bull. Seismol. Soc. Am.* **108**, no. 5,
763 2675-2686, doi: 10.1785/0120180023.

764 Zhao, D., K. Yamashita, and G. Toyokuni (2018) Tomography of the 2016 Kumamoto
765 earthquake area and the Beppu-Shimabara graben, *Sci. Rep.* **8**, 15488, doi: 10.1038/s41598-
766 018-33805-0.

767

768 **Full mailing address for each author**

769 Disaster Prevention Research Institute, Kyoto University

770 Gokasho, Uji, Kyoto 611-0011, Japan

771 (K.A. and T.I.)

772

773 ***Corresponding author:**

774 Kimiyuki Asano (k-asano@sms.dpri.kyoto-u.ac.jp)

775

776

777 **Tables**

778

779 **Table 1.** Representation of fault models during kinematic waveform inversion analysis.

Fault segment	H1	H2	F1	F2	F3
Upper south corner	32.6550°N 130.7554°E	32.6550°N 130.7554°E	32.7722°N 130.8072°E	32.8668°N 130.9697°E	32.8890°N 130.9937°E
Strike/dip	201°/62°	201°/90°	235°/66°	228°/67°	239°/69°
Length	16.0 km	16.0 km	18.0 km	4.0 km	6.0 km
Width	13.1 km	6.0 km	19.1 km	19.1 km	19.1 km
Top depth	6.6 km	0.6 km	0.4 km	0.5 km	0.2 km
Bottom depth	18.2 km	6.6 km	17.9 km	17.9 km	18.1 km
Point-source interval	0.22 km × 0.22 km				
Number of point sources	4248	1944	6966	1542	2322
Control-point interval	2.0 km × 2.0 km				
Number of control points	56	24	90	20	30
Number of time windows	9				
Duration / time shift of the time window	1.0 s / 0.5 s				

780

781 **Figure Captions**

782 **Figure 1.** Index map of the study area. Sold triangles indicate the locations of strong motion
783 stations used for the kinematic source inversion. The epicenter of the 2016 Kumamoto
784 mainshock (Mitsuoka *et al.*, 2020) is represented by the solid star. Black broken rectangles
785 correspond to the surface projection of source fault models used for the kinematic waveform
786 inversion analysis and thick black solid lines indicate the top of the fault plane. Red lines
787 represent active fault traces compiled by Nakata and Imaizumi (2002). RTL indicates the
788 Rokkoku Tectonic Line (Yanagida, 1958). The inset map indicates the location of the study
789 area in the Japanese archipelago.

790

791 **Figure 2.** Schematic illustration of the discretization of the source fault plane and locations of
792 the control points (large solid circles) to which unknown model parameters were assigned
793 during the kinematic waveform inversion. The dense distribution of point sources for the
794 calculation of Green's functions is depicted by small solid circles.

795

796 **Figure 3.** (a) Epicenters of the aftershocks determined by Mitsuoka *et al.* (2020) within 6 hours
797 from the mainshock (colored circles) and the assumed source fault model (solid rectangles).
798 The purple lines represent the surface rupture traces compiled by Kumahara *et al.* (2016).
799 (b) The vertical cross section of the aftershocks and the source fault plane around the Hinagu

800 Fault. (c) The vertical cross section of the aftershocks and the source fault plane around the
801 Futagawa Fault.

802

803 **Figure 4.** (a) Distribution of the final slip amounts on the source fault planes with slip vectors.

804 The contour interval of the slip is 1 m. The arrow shows the slip vector of the hanging wall
805 relative to the foot wall. The open star indicates the hypocenter or rupture starting point.

806 Dashed lines correspond to boundaries of fault segments with different strike and dip angles.

807 (b) Slip velocity functions obtained for every control point. The maximum slip velocity is

808 3.1 m/s.

809

810 **Figure 5.** Comparison between observed velocity waveforms (gray) and synthetic waveforms

811 (black) in the frequency range of 0.05–1 Hz. The maximum absolute amplitude of the

812 observed waveform is shown above each trace (unit: cm/s). EW: east–west, NS: north–

813 south, UD: up–down.

814

815 **Figure 6.** Snapshots of the slip velocity every 1 s. The open star indicates the rupture starting

816 point. Dashed lines correspond to boundaries of fault segments with different strike and dip

817 angles.

818

819 **Figure 7.** Map view of the estimated final slip distribution. The solid triangles indicate strong
820 motion stations in the near-source area, which were referred to in this paper. Red lines
821 represent active fault traces compiled by Nakata and Imaizumi (2002), and blue lines
822 represent surface ruptures associated the 2016 Kumamoto earthquake compiled by
823 Kumahara *et al.* (2016).

824

825 **Figure 8.** (a) Slip velocity functions at control points on the Futagawa fault segments for each
826 depth bin. Slip velocity functions of the same depth bin were aligned by the peak time,
827 which correspond to 0 s in the plots. (b) Relationship between peak time from the onset
828 time and peak slip velocity for each depth bin. The weight average of the peak time is
829 indicated in each plot.

830

831 **Figure 9.** Simulated and observed (a) velocity and (b) displacement waveforms at three near-
832 fault strong motion stations (93011, 93048, and 93051). The numerical value above each
833 trace indicates the maximum absolute amplitude of the observed waveform.

834

835 **Figure 10.** (a) Displacements observed during 30 s after the origin time at two strong motion
836 stations in the Aso Valley (KMMH04 and 93002). Crosses and associated numbers indicate
837 the lapsed time in seconds with respect to the origin. The thick arrow indicates the direction

838 normal to the strike angle of the Futagawa fault. (b) Simulated and observed velocity
839 waveforms for stations KMMH04 and 93002. The numerical value above each trace
840 indicates the maximum absolute amplitude of the observed waveform in cm/s.
841

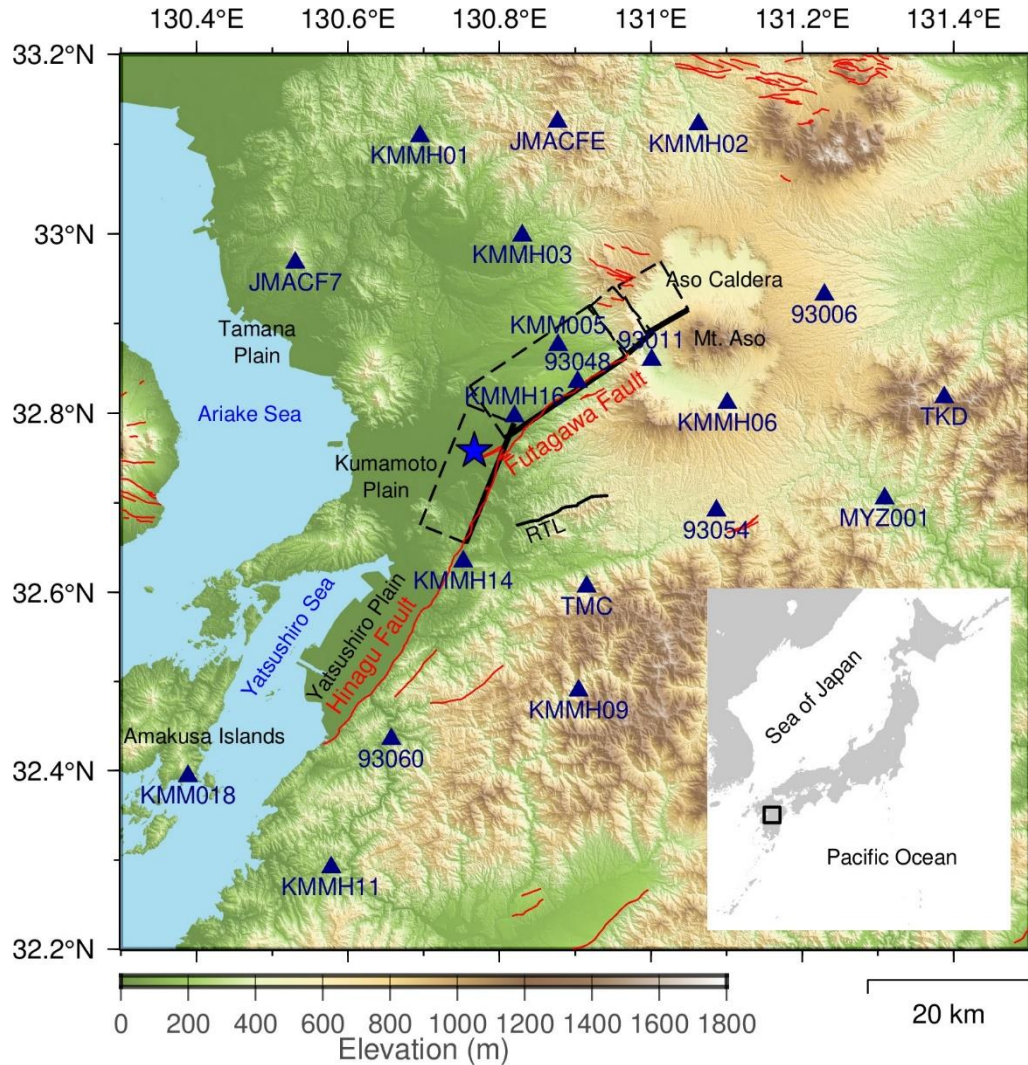


Figure 1. Index map of the study area. Solid triangles indicate the locations of strong motion stations used for the kinematic source inversion. The epicenter of the 2016 Kumamoto mainshock (Mitsuoka *et al.*, 2020) is represented by the solid star. Black broken rectangles correspond to the surface projection of source fault models used for the kinematic waveform inversion analysis and thick black solid lines indicate the top of the fault plane. Red lines represent active fault traces compiled by Nakata and Imaizumi (2002). RTL indicates the Rikkoku Tectonic Line (Yanagida, 1958). The inset map indicates the location of the study area in the Japanese archipelago.

Ground Surface

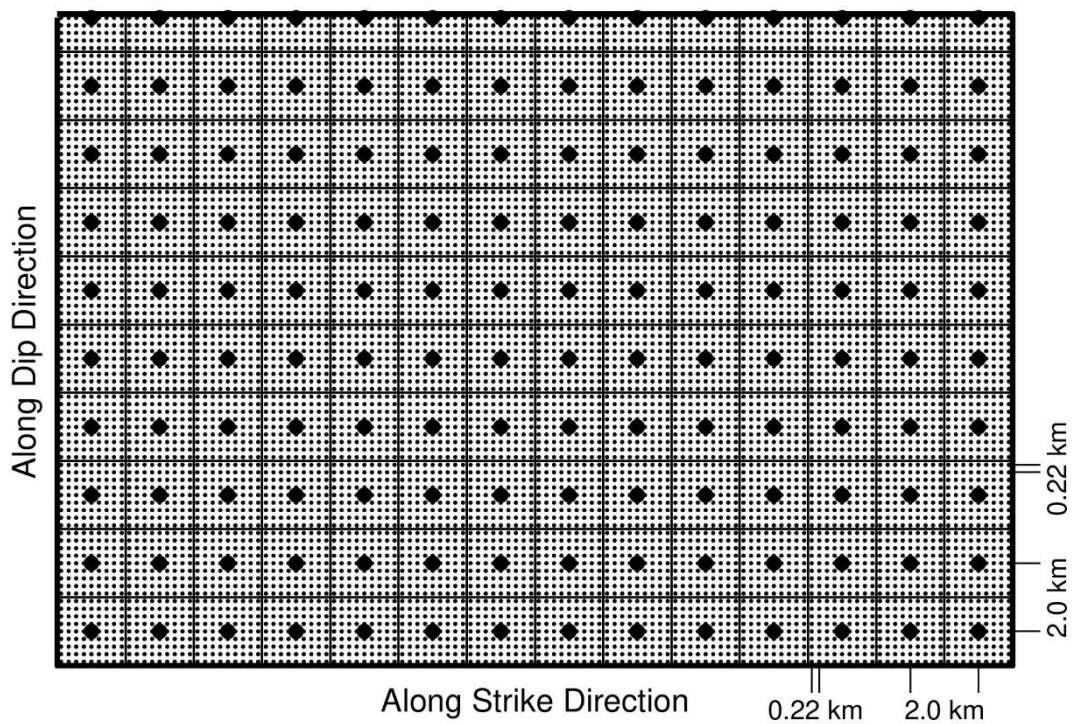


Figure 2. Schematic illustration of the discretization of the source fault plane and locations of the control points (large solid circles) to which unknown model parameters were assigned during the kinematic waveform inversion. The dense distribution of point sources for the calculation of Green's functions is depicted by small solid circles.

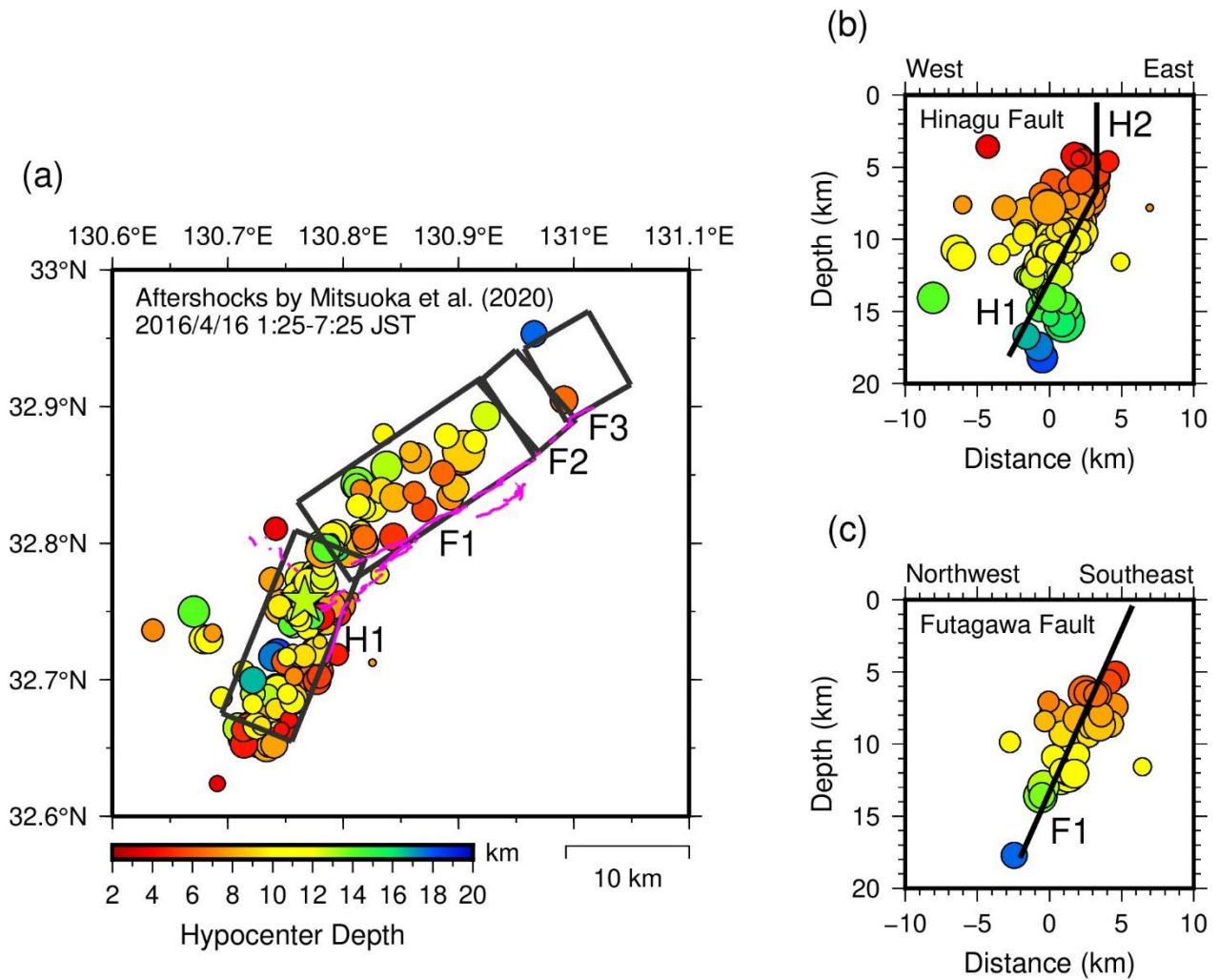


Figure 3. (a) Epicenters of the aftershocks determined by Mitsuoka *et al.* (2020) within 6 hours from the mainshock (colored circles) and the assumed source fault model (solid rectangles). The purple lines represent the surface rupture traces compiled by Kumahara *et al.* (2016). (b) The vertical cross section of the aftershocks and the source fault plane around the Hinagu Fault. (c) The vertical cross section of the aftershocks and the source fault plane around the Futagawa Fault.

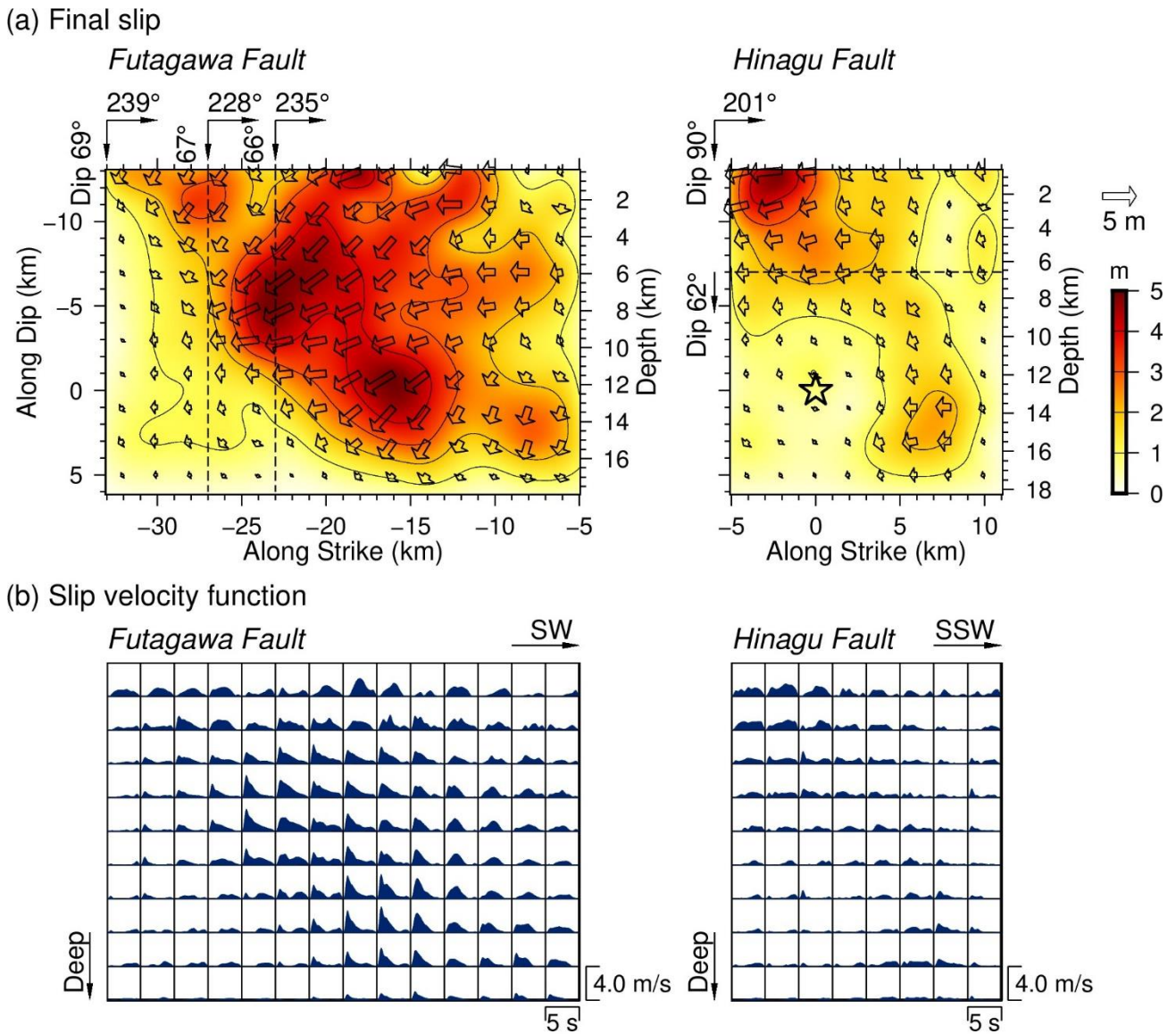


Figure 4. (a) Distribution of the final slip amounts on the source fault planes with slip vectors. The contour interval of the slip is 1 m. The arrow shows the slip vector of the hanging wall relative to the foot wall. The open star indicates the hypocenter or rupture starting point. Dashed lines correspond to boundaries of fault segments with different strike and dip angles. (b) Slip velocity functions obtained for every control point. The maximum slip velocity is 3.1 m/s.

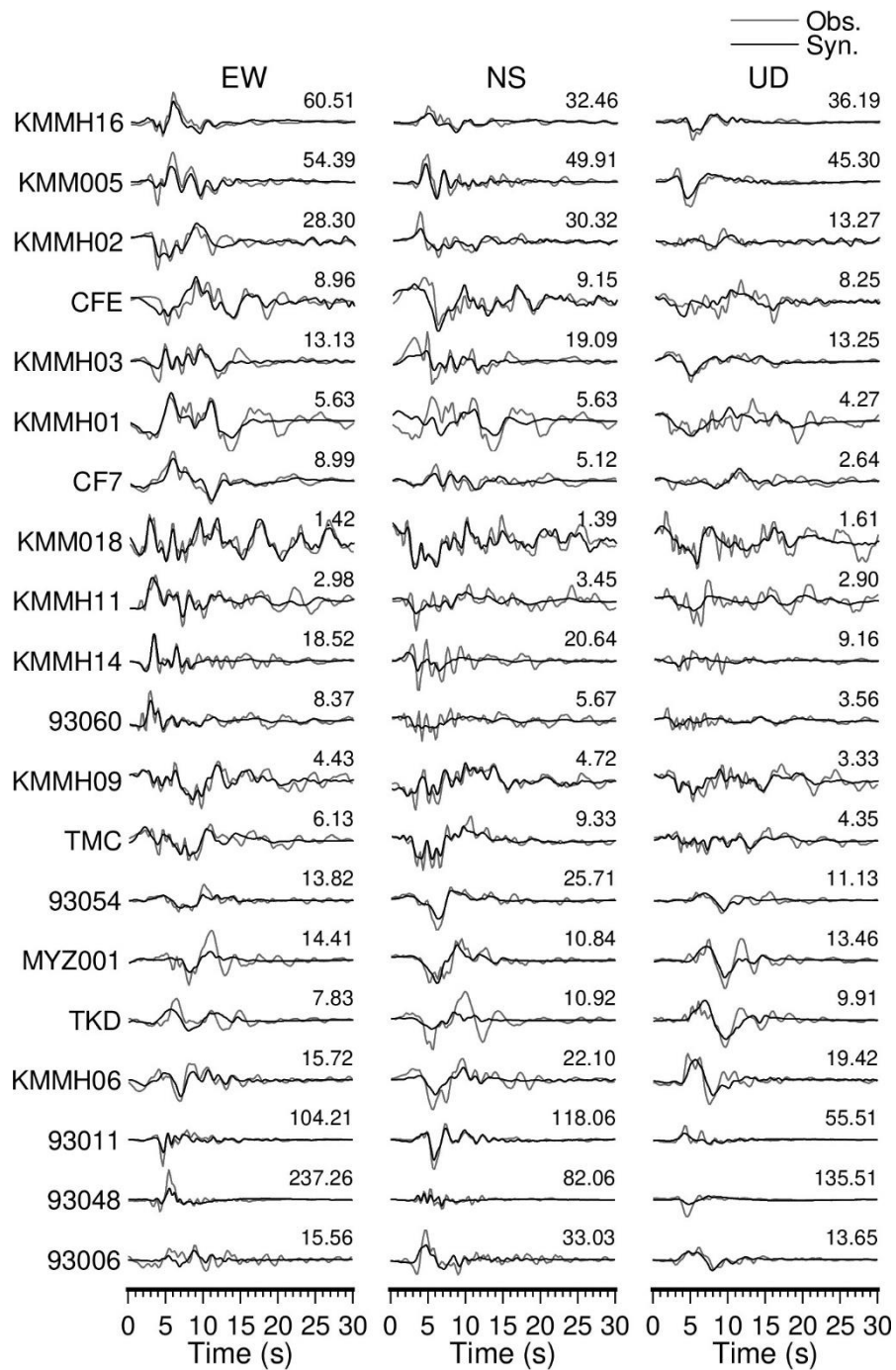


Figure 5. Comparison between observed velocity waveforms (gray) and synthetic waveforms (black) in the frequency range of 0.05–1 Hz. The maximum absolute amplitude of the observed waveform is shown above each trace (unit: cm/s). EW: east–west, NS: north–south, UD: up–down.

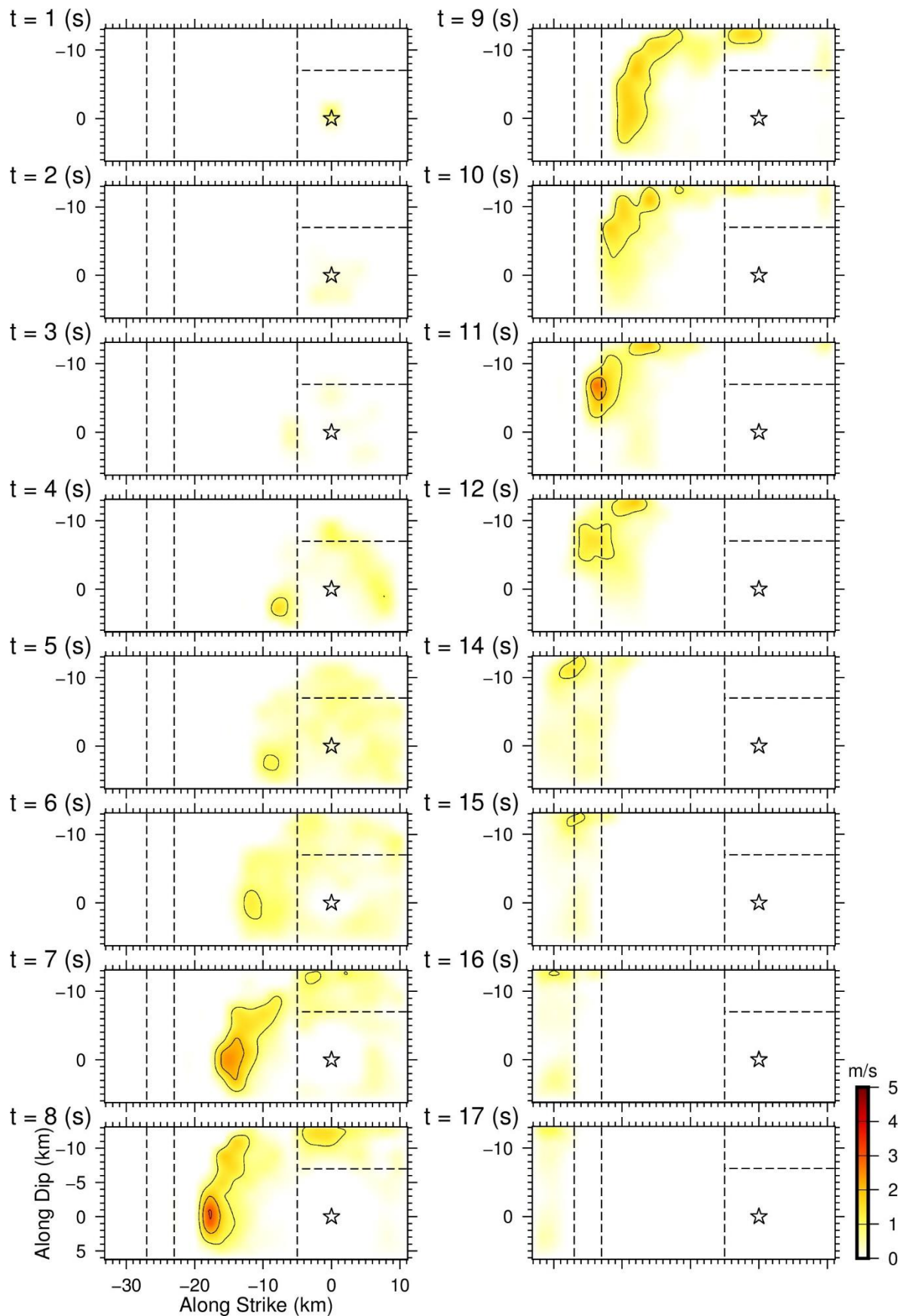


Figure 6. Snapshots of the slip velocity at every 1 s. The open star indicates the rupture starting point. Dashed lines correspond to boundaries of fault segments with different strike and dip angles.

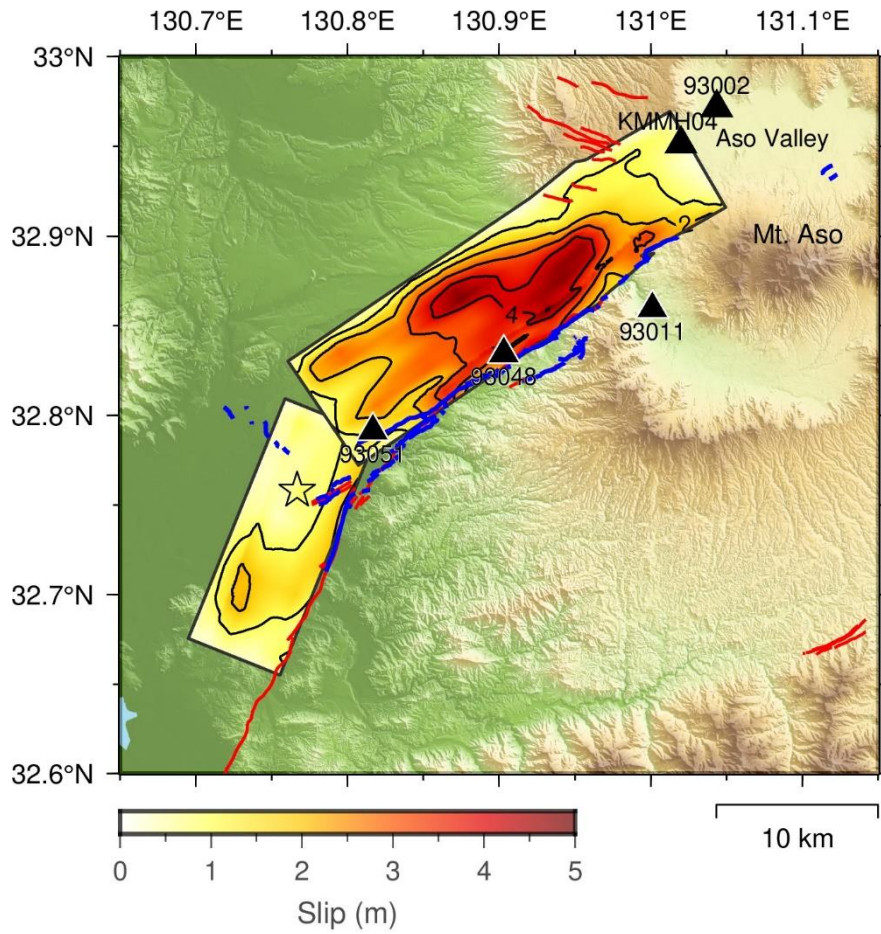
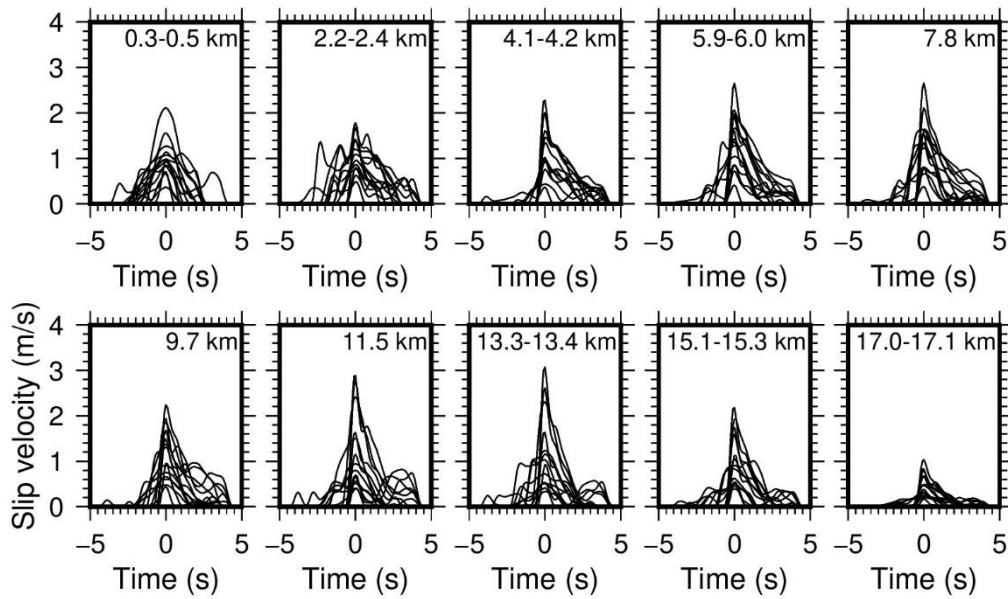


Figure 7. Map view of the estimated final slip distribution. The solid triangles indicate strong motion stations in the near-source area, which were referred to in this paper. Red lines represent active fault traces compiled by Nakata and Imaizumi (2002), and blue lines represent surface ruptures associated the 2016 Kumamoto earthquake compiled by Kumahara et al. (2016).

(a) Slip velocity functions aligned by the peak time



(b) Peak slip velocity vs. peak time

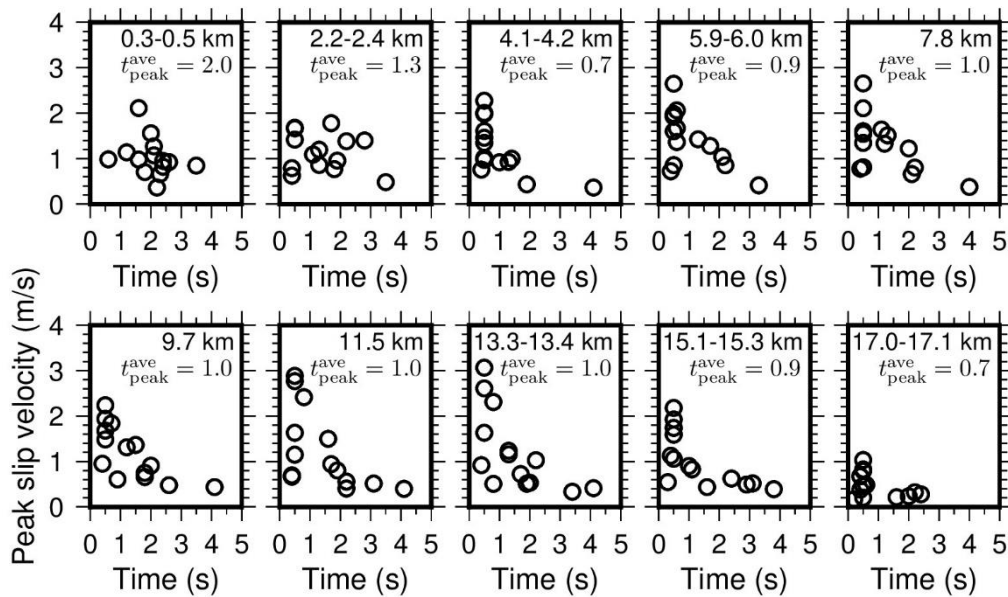


Figure 8. (a) Slip velocity functions at control points on the Futagawa fault segments for each depth bin. Slip velocity functions of the same depth bin were aligned by the peak time, which correspond to 0 s in the plots. (b) Relationship between peak time from the onset time and peak slip velocity for each depth bin. The weight average of the peak time is indicated in each plot.

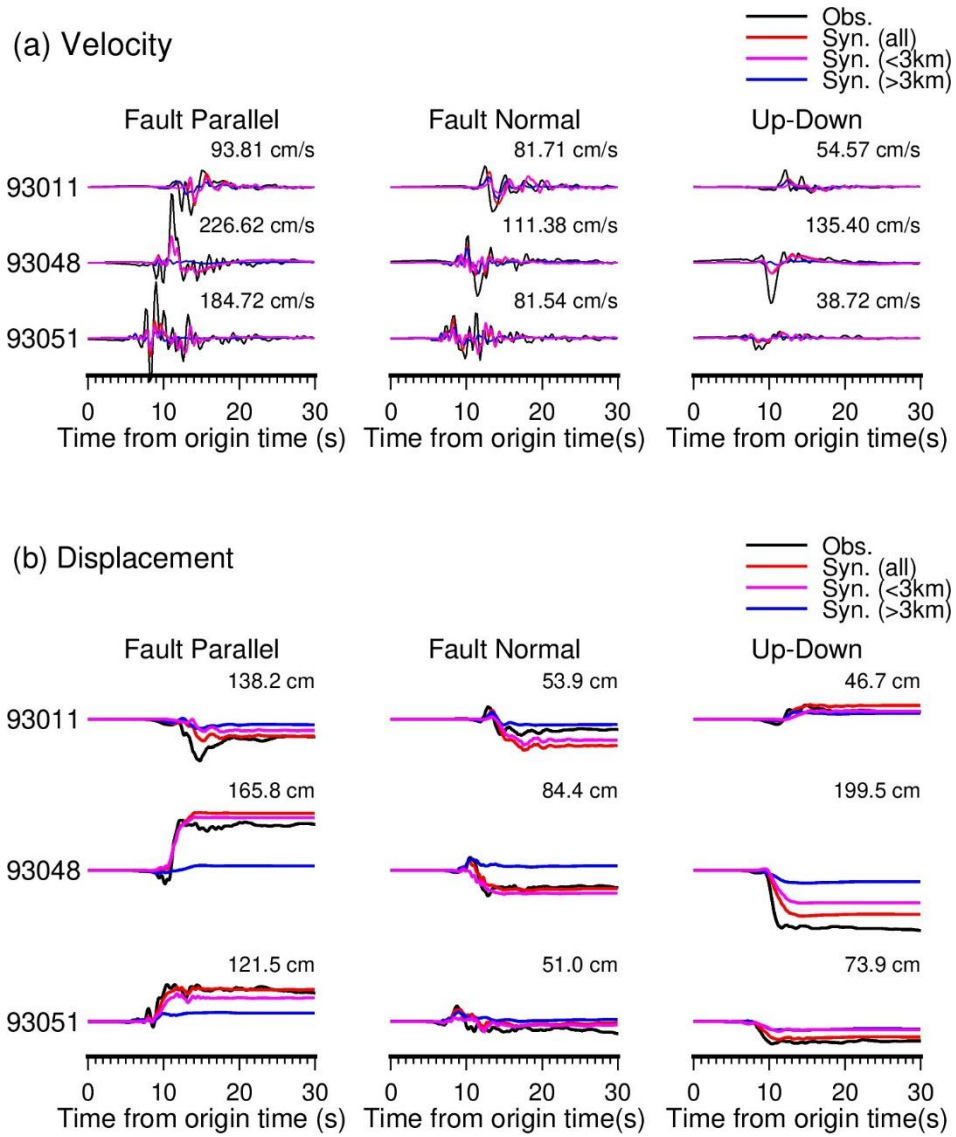


Figure 9. Simulated and observed (a) velocity and (b) displacement waveforms at three near-fault strong motion stations (93011, 93048, and 93051). The numerical value above each trace indicates the maximum absolute amplitude of the observed waveform.

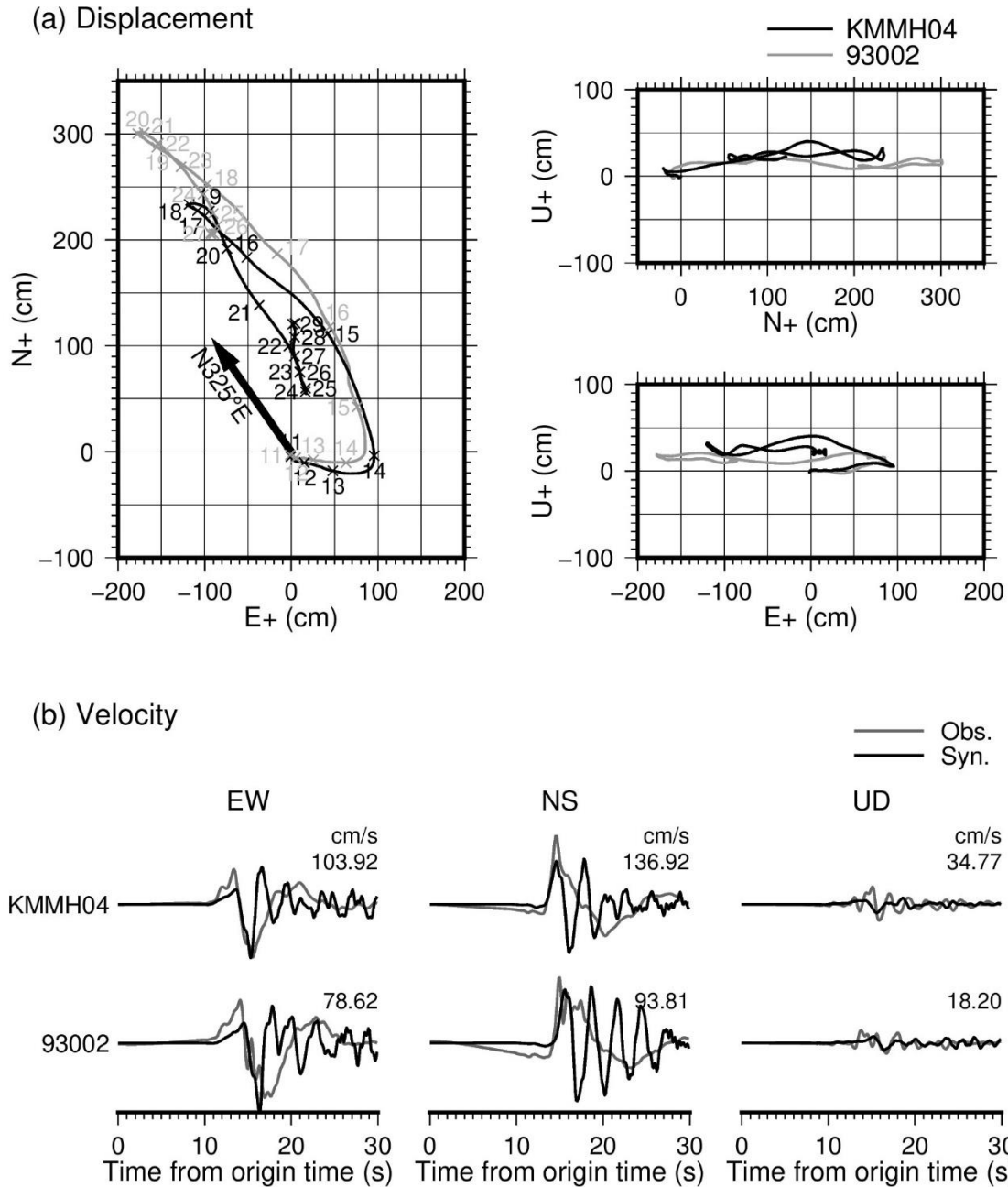


Figure 10. (a) Displacements observed during 30 s after the origin time at two strong motion stations in the Aso Valley (KMMH04 and 93002). Crosses and associated numbers indicate the lapsed time in seconds with respect to the origin time. The thick arrow indicates the direction normal to the strike angle of the Futagawa fault. (b) Simulated and observed velocity waveforms for stations KMMH04 and 93002. The numerical value above each trace indicates the maximum absolute amplitude of the observed waveform in cm/s.

Supplemental material to

Revisiting the source rupture process of the mainshock of the 2016 Kumamoto earthquake and implications for the generation of near-fault ground motions and forward directivity pulses

Kimiyuki Asano and Tomotaka Iwata

This electronic supplement contains the velocity structure models of each strong motion station used for this study.

Table S1. Velocity structure model for KMM005.

Top depth (m)	V_p (m/s)	V_s (m/s)	Density (kg/m ³)	Q_p	Q_s
0.00	1401	100	1753	102	60
4.38	1429	125	1764	102	60
5.25	1456	150	1774	102	60
5.26	1484	175	1785	102	60
5.27	1512	200	1795	102	60
7.75	1540	225	1805	102	60
7.75	1568	250	1816	102	60
7.75	1595	275	1826	102	60
7.76	1600	300	1840	102	60
9.42	1600	350	1850	102	60
13.31	1600	400	1850	102	60
20.27	1700	450	1900	102	60
20.35	1800	500	1900	102	60
27.98	2000	600	1900	170	100
47.22	2500	1100	2150	255	150
425.91	4000	2100	2400	340	200
1020.79	5000	2700	2500	340	200
1220.80	5500	3100	2600	510	300
3981.30	5800	3400	2700	680	400
16471.80	6400	3800	2800	680	400
32641.00	7500	4500	3200	850	500

Table S2. Velocity structure model for KMM018.

Top depth (m)	V_p (m/s)	V_s (m/s)	Density (kg/m ³)	Q_p	Q_s
0.00	1600	350	1850	102	60
2.70	1600	400	1850	102	60
5.83	1700	450	1900	102	60
6.98	1800	500	1900	102	60
24.49	2000	600	1900	170	100
45.86	2400	900	2050	170	100
192.07	3400	1600	2300	255	150
419.31	5000	2700	2500	340	200
657.64	5500	3100	2600	510	300
4203.10	5800	3400	2700	680	400
16930.40	6400	3800	2800	680	400
32079.30	7500	4500	3200	850	500

Table S3. Velocity structure model for KMMH01.

Top depth (m)	V_p (m/s)	V_s (m/s)	Density (kg/m ³)	Q_p	Q_s
0.00	1401	100	1753	102	60
0.10	1429	125	1764	102	60
0.25	1456	150	1774	102	60
0.50	1484	175	1785	102	60
0.75	1512	200	1795	102	60
1.00	1540	225	1805	102	60
1.25	1568	250	1816	102	60
1.50	1595	275	1826	102	60
2.00	1600	300	1840	102	60
3.00	1600	350	1850	102	60
3.50	1600	400	1850	102	60
4.00	1700	450	1900	102	60
5.00	2000	600	1900	170	100
6.24	2500	1100	2150	255	150
8.42	3000	1400	2250	255	150
18.74	3500	1700	2300	255	150
23.50	4000	2100	2400	340	200
28.14	4000	2100	2400	340	200
56.01	5000	2700	2500	340	200
81.26	5500	3100	2600	510	300
3644.50	5800	3400	2700	680	400
13493.00	6400	3800	2800	680	400
32011.60	7500	4500	3200	850	500

Table S4. Velocity structure model for KMMH02.

Top depth (m)	V_p (m/s)	V_s (m/s)	Density (kg/m ³)	Q_p	Q_s
0.00	1401	100	1753	102	60
0.10	1429	125	1764	102	60
0.25	1456	150	1774	102	60
0.50	1484	175	1785	102	60
0.75	1512	200	1795	102	60
1.00	1540	225	1805	102	60
1.25	1568	250	1816	102	60
1.50	1595	275	1826	102	60
2.00	1600	300	1840	102	60
3.00	1600	350	1850	102	60
3.50	1600	400	1850	102	60
4.00	1700	450	1900	102	60
5.00	2500	1100	2150	255	150
354.82	3000	1400	2250	255	150
1318.84	4000	2100	2400	340	200
1318.85	5000	2700	2500	340	200
1319.44	5500	3100	2600	510	300
4604.70	5800	3400	2700	680	400
14000.50	6400	3800	2800	680	400
33291.00	7500	4500	3200	850	500

Table S5. Velocity structure model for KMMH03.

Top depth (m)	V_p (m/s)	V_s (m/s)	Density (kg/m ³)	Q_p	Q_s
0.00	1401	100	1753	102	60
0.10	1429	125	1764	102	60
0.25	1456	150	1774	102	60
0.50	1484	175	1785	102	60
0.75	1512	200	1795	102	60
1.00	1540	225	1805	102	60
1.25	1568	250	1816	102	60
1.50	1595	275	1826	102	60
2.00	1600	300	1840	102	60
3.00	1600	350	1850	102	60
3.50	1600	400	1850	102	60
4.00	1700	450	1900	102	60
5.00	2000	600	1900	170	100
17.81	2400	900	2050	170	100
21.28	2500	1100	2150	255	150
381.37	4000	2100	2400	340	200
387.16	4000	2100	2400	340	200
389.32	5000	2700	2500	340	200
390.75	5500	3100	2600	510	300
4209.10	5800	3400	2700	680	400
16444.00	6400	3800	2800	680	400
32198.10	7500	4500	3200	850	500

Table S6. Velocity structure model for KMMH06.

Top depth (m)	V_p (m/s)	V_s (m/s)	Density (kg/m ³)	Q_p	Q_s
0.00	1401	100	1753	102	60
3.81	1512	200	1795	102	60
5.76	1600	300	1840	102	60
7.05	1600	350	1850	102	60
8.17	1600	400	1850	102	60
11.25	1700	450	1900	102	60
16.58	1800	500	1900	102	60
61.61	2000	600	1900	170	100
76.54	2500	1100	2150	255	150
386.31	4000	2100	2400	340	200
518.46	5000	2700	2500	340	200
718.46	5500	3100	2600	510	300
3741.60	5800	3400	2700	680	400
15264.90	6400	3800	2800	680	400
34533.60	7500	4500	3200	850	500

Table S7. Velocity structure model for KMMH09.

Top depth (m)	V_p (m/s)	V_s (m/s)	Density (kg/m ³)	Q_p	Q_s
0.00	1401	100	1753	102	60
0.10	1429	125	1764	102	60
0.25	1456	150	1774	102	60
0.50	1484	175	1785	102	60
0.75	1512	200	1795	102	60
1.00	1540	225	1805	102	60
1.25	1568	250	1816	102	60
1.50	1595	275	1826	102	60
2.00	1600	300	1840	102	60
3.00	1600	350	1850	102	60
3.50	1600	400	1850	102	60
4.00	1700	450	1900	102	60
5.00	2000	600	1900	170	100
148.66	4000	2100	2400	340	200
158.31	4000	2100	2400	340	200
445.12	5000	2700	2500	340	200
457.70	5500	3100	2600	510	300
1912.60	5800	3400	2700	680	400
17609.60	6400	3800	2800	680	400
35973.00	7500	4500	3200	850	500

Table S8. Velocity structure model for KMMH11.

Top depth (m)	V_p (m/s)	V_s (m/s)	Density (kg/m ³)	Q_p	Q_s
0.00	1401	100	1753	102	60
0.10	1429	125	1764	102	60
0.25	1456	150	1774	102	60
0.50	1484	175	1785	102	60
0.75	1512	200	1795	102	60
1.00	1540	225	1805	102	60
1.25	1568	250	1816	102	60
1.50	1595	275	1826	102	60
2.00	1600	300	1840	102	60
3.00	1600	350	1850	102	60
3.50	1600	400	1850	102	60
4.00	1700	450	1900	102	60
5.00	2000	600	1900	170	100
8.50	2400	900	2050	170	100
12.87	2500	1100	2150	255	150
27.39	3000	1400	2250	255	150
34.17	3400	1600	2300	255	150
42.91	3500	1700	2300	255	150
50.11	4000	2100	2400	340	200
80.07	4000	2100	2400	340	200
104.04	5000	2700	2500	340	200
140.06	5500	3100	2600	510	300
3291.00	5800	3400	2700	680	400
17532.40	6400	3800	2800	680	400
33488.20	7500	4500	3200	850	500

Table S9. Velocity structure model for KMMH14.

Top depth (m)	V_P (m/s)	V_S (m/s)	Density (kg/m ³)	Q_P	Q_S
0.00	1401	100	1753	102	60
3.97	1429	125	1764	102	60
4.00	1456	150	1774	102	60
4.29	1484	175	1785	102	60
9.83	1512	200	1795	102	60
9.90	1568	250	1816	102	60
9.90	1600	300	1840	102	60
20.58	1700	450	1900	102	60
83.35	4000	2100	2400	340	200
359.90	4000	2100	2400	340	200
362.73	5500	3100	2600	510	300
1938.30	5800	3400	2700	680	400
16074.60	6400	3800	2800	680	400
33428.10	7500	4500	3200	850	500

Table S10. Velocity structure model for KMMH16.

Top depth (m)	V_P (m/s)	V_S (m/s)	Density (kg/m ³)	Q_P	Q_S
0.00	1401	100	1753	102	60
9.13	1484	175	1785	102	60
9.43	1512	200	1795	102	60
18.68	1595	275	1826	102	60
18.73	1600	300	1840	102	60
23.25	1600	350	1850	102	60
27.34	1600	400	1850	102	60
52.20	2000	600	1900	170	100
80.04	2400	900	2050	170	100
315.82	2500	1100	2150	255	150
577.81	4000	2100	2400	340	200
1441.82	5000	2700	2500	340	200
1641.82	5500	3100	2600	510	300
3293.50	5800	3400	2700	680	400
16250.70	6400	3800	2800	680	400
32284.70	7500	4500	3200	850	500

Table S11. Velocity structure model for MYZ001.

Top depth (m)	V_p (m/s)	V_s (m/s)	Density (kg/m ³)	Q_p	Q_s
0.00	1401	100	1753	102	60
0.10	1429	125	1764	102	60
0.25	1456	150	1774	102	60
0.50	1484	175	1785	102	60
0.75	1512	200	1795	102	60
1.00	1540	225	1805	102	60
1.25	1568	250	1816	102	60
1.50	1595	275	1826	102	60
2.00	1600	300	1840	102	60
3.00	1600	350	1850	102	60
3.50	1600	400	1850	102	60
4.00	1700	450	1900	102	60
5.00	3000	1400	2250	255	150
11.99	3500	1700	2300	255	150
21.98	4000	2100	2400	340	200
32.57	4000	2100	2400	340	200
77.83	5000	2700	2500	340	200
106.46	5500	3100	2600	510	300
2883.40	5800	3400	2700	680	400
16774.40	6400	3800	2800	680	400
33854.70	7500	4500	3200	850	500

Table S12. Velocity structure model for 93006.

Top depth (m)	V_p (m/s)	V_s (m/s)	Density (kg/m ³)	Q_p	Q_s
0.00	1401	100	1753	102	60
2.31	1456	150	1774	102	60
2.38	1484	175	1785	102	60
8.90	1512	200	1795	102	60
10.52	1600	300	1840	102	60
20.56	1600	350	1850	102	60
22.31	1600	400	1850	102	60
25.67	1700	450	1900	102	60
26.06	2000	600	1900	170	100
49.83	2500	1100	2150	255	150
191.22	3000	1400	2250	255	150
201.67	4000	2100	2400	340	200
524.48	4000	2100	2400	340	200
599.00	5500	3100	2600	510	300
3648.20	5800	3400	2700	680	400
14139.30	6400	3800	2800	680	400
34033.90	7500	4500	3200	850	500

Table S13. Velocity structure model for 93011.

Top depth (m)	V_P (m/s)	V_S (m/s)	Density (kg/m ³)	Q_P	Q_S
0.00	1401	100	1753	102	60
5.67	1512	200	1795	102	60
7.73	1540	225	1805	102	60
12.35	1568	250	1816	102	60
13.98	1595	275	1826	102	60
15.26	1600	300	1840	102	60
18.69	1600	350	1850	102	60
23.33	1600	400	1850	102	60
81.41	1700	450	1900	102	60
97.26	2000	600	1900	170	100
136.03	2500	1100	2150	255	150
617.97	4000	2100	2400	340	200
1403.37	5000	2700	2500	340	200
1603.37	5500	3100	2600	510	300
4173.90	5800	3400	2700	680	400
15757.20	6400	3800	2800	680	400
34002.20	7500	4500	3200	850	500

Table S14. Velocity structure model for 93048.

Top depth (m)	V_P (m/s)	V_S (m/s)	Density (kg/m ³)	Q_P	Q_S
0.00	1401	100	1753	102	60
10.01	1512	200	1795	102	60
18.75	1600	300	1840	102	60
23.92	1600	350	1850	102	60
29.88	1600	400	1850	102	60
46.15	1700	450	1900	102	60
46.15	2500	1100	2150	255	150
189.10	4000	2100	2400	340	200
1139.22	5000	2700	2500	340	200
1339.22	5500	3100	2600	510	300
3849.10	5800	3400	2700	680	400
16012.10	6400	3800	2800	680	400
33083.60	7500	4500	3200	850	500

Table S15. Velocity structure model for 93054.

Top depth (m)	V_P (m/s)	V_S (m/s)	Density (kg/m ³)	Q_P	Q_S
0.00	1401	100	1753	102	60
0.10	1429	125	1764	102	60
0.25	1456	150	1774	102	60
0.50	1484	175	1785	102	60
0.75	1512	200	1795	102	60
1.00	1540	225	1805	102	60
1.25	1568	250	1816	102	60
1.50	1595	275	1826	102	60
2.00	1600	300	1840	102	60
3.00	1600	350	1850	102	60
3.50	1600	400	1850	102	60
4.00	1700	450	1900	102	60
5.00	2000	600	1900	170	100
7.40	2500	1100	2150	255	150
84.98	4000	2100	2400	340	200
92.18	4000	2100	2400	340	200
364.85	5500	3100	2600	510	300
2933.30	5800	3400	2700	680	400
16525.90	6400	3800	2800	680	400
35317.10	7500	4500	3200	850	500

Table S16. Velocity structure model for 93060.

Top depth (m)	V_p (m/s)	V_s (m/s)	Density (kg/m ³)	Q_p	Q_s
0.00	1401	100	1753	102	60
0.56	1429	125	1764	102	60
3.17	1456	150	1774	102	60
4.46	1512	200	1795	102	60
6.27	1600	300	1840	102	60
7.76	2500	1100	2150	255	150
10.68	3000	1400	2250	255	150
21.09	3500	1700	2300	255	150
31.26	4000	2100	2400	340	200
79.78	5000	2700	2500	340	200
127.84	5500	3100	2600	510	300
2507.40	5800	3400	2700	680	400
16588.10	6400	3800	2800	680	400
33673.20	7500	4500	3200	850	500

Table S17. Velocity structure model for JMACF7.

Top depth (m)	V_p (m/s)	V_s (m/s)	Density (kg/m ³)	Q_p	Q_s
0.00	1401	100	1753	102	60
0.10	1429	125	1764	102	60
0.25	1456	150	1774	102	60
0.50	1484	175	1785	102	60
0.75	1512	200	1795	102	60
1.00	1540	225	1805	102	60
1.25	1568	250	1816	102	60
1.50	1595	275	1826	102	60
2.00	1600	300	1840	102	60
3.00	1600	350	1850	102	60
3.50	1600	400	1850	102	60
4.00	1700	450	1900	102	60
5.00	2000	600	1900	170	100
13.07	2500	1100	2150	255	150
36.24	3000	1400	2250	255	150
36.41	3500	1700	2300	255	150
36.58	4000	2100	2400	340	200
371.04	4000	2100	2400	340	200
387.85	5000	2700	2500	340	200
391.41	5500	3100	2600	510	300
2861.80	5800	3400	2700	680	400
14888.30	6400	3800	2800	680	400
32164.30	7500	4500	3200	850	500

Table S18. Velocity structure model for JMACFE.

Top depth (m)	V_p (m/s)	V_s (m/s)	Density (kg/m ³)	Q_p	Q_s
0.00	1401	100	1753	102	60
0.10	1429	125	1764	102	60
0.25	1456	150	1774	102	60
0.50	1484	175	1785	102	60
0.75	1512	200	1795	102	60
1.00	1540	225	1805	102	60
1.25	1568	250	1816	102	60
1.50	1595	275	1826	102	60
2.00	1600	300	1840	102	60
3.00	1600	350	1850	102	60
3.50	1600	400	1850	102	60
4.00	1700	450	1900	102	60
5.00	2500	1100	2150	255	150
1042.69	3000	1400	2250	255	150
1643.99	4000	2100	2400	340	200
1644.04	5500	3100	2600	510	300
4585.00	5800	3400	2700	680	400
13491.70	6400	3800	2800	680	400
32853.20	7500	4500	3200	850	500

Table S19. Velocity structure model for TMC.

Top depth (m)	V_p (m/s)	V_s (m/s)	Density (kg/m ³)	Q_p	Q_s
0.00	1401	100	1753	102	60
0.10	1429	125	1764	102	60
0.25	1456	150	1774	102	60
0.50	1484	175	1785	102	60
0.75	1512	200	1795	102	60
1.00	1540	225	1805	102	60
1.25	1568	250	1816	102	60
1.50	1595	275	1826	102	60
2.00	1600	300	1840	102	60
3.00	1600	350	1850	102	60
3.50	1600	400	1850	102	60
4.00	1700	450	1900	102	60
5.00	2500	1100	2150	255	150
8.16	3000	1400	2250	255	150
19.27	3500	1700	2300	255	150
30.53	4000	2100	2400	340	200
35.19	4000	2100	2400	340	200
186.52	5000	2700	2500	340	200
230.31	5500	3100	2600	510	300
1862.60	5800	3400	2700	680	400
17081.50	6400	3800	2800	680	400
35413.20	7500	4500	3200	850	500

Table S20. Velocity structure model for TKD.

Top depth (m)	V_p (m/s)	V_s (m/s)	Density (kg/m ³)	Q_p	Q_s
0.00	1401	100	1753	102	60
0.10	1429	125	1764	102	60
0.25	1456	150	1774	102	60
0.50	1484	175	1785	102	60
0.75	1512	200	1795	102	60
1.00	1540	225	1805	102	60
1.25	1568	250	1816	102	60
1.50	1595	275	1826	102	60
2.00	1600	300	1840	102	60
3.00	1600	350	1850	102	60
3.50	1600	400	1850	102	60
4.00	1700	450	1900	102	60
5.00	2500	1100	2150	255	150
19.86	3000	1400	2250	255	150
29.30	3500	1700	2300	255	150
45.88	4000	2100	2400	340	200
64.02	4000	2100	2400	340	200
126.32	5000	2700	2500	340	200
201.00	5500	3100	2600	510	300
2051.10	5800	3400	2700	680	400
16223.50	6400	3800	2800	680	400
33680.70	7500	4500	3200	850	500

Table S21. Velocity structure model for 93051.

Top depth (m)	V_p (m/s)	V_s (m/s)	Density (kg/m ³)	Q_p	Q_s
0.00	1401	100	1753	102	60
12.83	1512	200	1795	102	60
21.75	1595	275	1826	102	60
21.75	1600	300	1840	102	60
25.64	1600	350	1850	102	60
30.26	1600	400	1850	102	60
40.97	1800	500	1900	102	60
42.71	2000	600	1900	170	100
82.34	2400	900	2050	170	100
337.33	2500	1100	2150	255	150
584.13	4000	2100	2400	340	200
1425.66	5000	2700	2500	340	200
1625.66	5500	3100	2600	510	300
3246.30	5800	3400	2700	680	400
16253.40	6400	3800	2800	680	400
32289.80	7500	4500	3200	850	500

Table S22. Velocity structure model for KMMH04.

Top depth (m)	V_p (m/s)	V_s (m/s)	Density (kg/m ³)	Q_p	Q_s
0.00	1401	100	1753	102	60
32.32	1456	150	1774	102	60
48.41	1484	175	1785	102	60
48.41	1512	200	1795	102	60
64.89	1595	275	1826	102	60
91.50	1600	300	1840	102	60
101.93	1600	350	1850	102	60
112.05	1600	400	1850	102	60
160.34	1700	450	1900	102	60
160.53	1800	500	1900	102	60
213.01	2000	600	1900	170	100
257.85	2500	1100	2150	255	150
412.61	3000	1400	2250	255	150
530.33	4000	2100	2400	340	200
1125.89	5000	2700	2500	340	200
1325.89	5500	3100	2600	510	300
4580.50	5800	3400	2700	680	400
16860.70	6400	3800	2800	680	400
33825.90	7500	4500	3200	850	500

Table S23. Velocity structure model for 93002.

Top depth (m)	V_p (m/s)	V_s (m/s)	Density (kg/m ³)	Q_p	Q_s
0.00	1401	100	1753	102	60
32.70	1484	175	1785	102	60
87.08	1512	200	1795	102	60
95.14	1540	225	1805	102	60
100.91	1568	250	1816	102	60
104.89	1595	275	1826	102	60
110.74	1600	300	1840	102	60
116.21	1600	350	1850	102	60
128.43	1600	400	1850	102	60
140.86	1700	450	1900	102	60
156.65	2500	1100	2150	255	150
496.31	3000	1400	2250	255	150
871.68	3500	1700	2300	255	150
871.71	4000	2100	2400	340	200
1222.87	5000	2700	2500	340	200
1422.87	5500	3100	2600	510	300
4550.30	5800	3400	2700	680	400
16602.00	6400	3800	2800	680	400
33810.80	7500	4500	3200	850	500